Electronic Supplementary Information

Cascade electrocatalysis *via* integration of ruthenium clusters and yttrium single atoms for a boosted alkaline hydrogen evolution reaction

Haotian Zhang,[a] Haoran Guo,*[b] Fuhui Zhang,[a] Jinyang Zhang,[a] Yizhuo Cheng,[c] Yanqing Ma,[cd] Lei Ma,[cde] and Limin Qi*[a]

[a]Beijing National Laboratory for Molecular Sciences (BNLMS), College of Chemistry and Molecular Engineering, Peking University, Beijing 100871, China.

[b]College of Chemistry, Key Laboratory for Green Organic Synthesis and Application of Hunan Province, Key Laboratory of Environmentally Friendly Chemistry and Application of Ministry of Education, Xiangtan University, Xiangtan 411105, China.

[c]Tianjin International Center for Nanoparticles and Nanosystems, Tianjin University, Tianjin 300072, China.

[d]Tianjin Key Laboratory of Low-dimensional Electronic Materials and Advanced Instrumentation, Tianjin University, Tianjin 300072, China.

[e]Haihe Laboratory for Low-dimensional Electronic Materials, Tianjin 300074, China.

*Corresponding authors: guohaoran@xtu.edu.cn, liminqi@pku.edu.cn

Materials and methods

1. Chemicals

Zinc (II) nitrate hexahydrate ($Zn(NO_3)_2$ $6H_2O$, 99%), hydrochloric acid (HCl, 36%), and sulfuric acid (H_2SO_4, 98%) were provided by Sinopharm Chemical Reagent Co., Ltd. Yttrium (III) acetylacetonate ($Y(acac)_3$, 99%), scandium (III) acetylacetonate ($Sc(acac)_3$, 99%), lanthanum (III) acetylacetonate ($La(acac)_3$, 99%), ruthenium (III) chloride trihydrate ($RuCl_3$ $3H_2O$, 98%), nickel (II) nitrate hexahydrate ($Ni(NO_3)_2$ $6H_2O$, 99%), iron (III) nitrate nonahydrate ($Fe(NO_3)_3$ $9H_2O$, 98%), and potassium thiocyanate (KSCN, 99%) were purchased from Shanghai Aladdin Biochemical Co., Ltd. 2-Methylimidazole (2-MeIm, 98%) and Nafion D521 solution (5 wt.%) were obtained from Sigma-Aldrich. Commercial Pt/C (20 wt.%) and Ru/C (5 wt.%) catalysts were bought from Shanghai Macklin Biochemical Industrial Co., Ltd. Urea ($(NH_2)_2CO$, 99%) was purchased from Xilong Scientific Co., Ltd. Ammonium fluoride (NH_4F, 99%), acetone, methanol, ethanol, isopropanol and potassium hydroxide (KOH, 95%) were obtained from Beijing Tongguang Fine Chemical Company. Hydrophilic carbon paper was purchased from the Kelude Experimental Equipment Technology Co., Ltd., and nickel foam (0.5 mm thickness) was purchased from Guangzhou Huayu Trading Co., Ltd. Anion exchange membrane (X37-50 Grade 60) was acquired from Dioxide Materials Sustainion. Deionized water with a resistivity of 18.2 MΩ cm was obtained from a Milli-Q System and used in all experiments.

2. Synthesis of $Y(acac)_3$@ZIF-8 and ZIF-8

The $Y(acac)_3$@ZIF-8 was synthesized based on the host-guest strategy. Typically, 4 mmol (1.19 g) $Zn(NO_3)_2$ $6H_2O$ and 0.4 mmol (0.154 g) $Y(acac)_3$ were dissolved in 15 mL of methanol, which was denoted as solution A. 16 mmol (1.314 g) 2-MeIm were dissolved in 10 mL of methanol as solution B. Then, solution B was rapidly mixed with solution A under magnetic stirring. After stirring for 8 h at room temperature, the white precipitate was collected by centrifugation, and washed with methanol for three

times and with ethanol for two times, followed by drying under vacuum at 60 ℃ overnight to obtain the $Y(acac)_3$@ZIF-8. The preparation process of the ZIF-8 was similar with that of the $Y(acac)_3$@ZIF-8 except for the absence of $Y(acac)_3$ in the precursor solution. The $Sc(acac)_3$@ZIF-8 and $La(acac)_3$@ZIF-8 were prepared using the similar method except for the use of $Sc(acac)_3$ and $La(acac)_3$ instead of $Y(acac)_3$ in the precursor solution, respectively.

3. Synthesis of YNC and NC

The $Y(acac)_3$@ZIF-8 (100 mg) was placed in a tube furnace for the pyrolysis treatment at 950 ℃ for 3 h in Ar atmosphere with a heating rate of 5 ℃ min^{-1}. Then the obtained black powders were washed with 1 M H_2SO_4 at 80 ℃ for 12 h for the acid treatment. After sufficient washing and centrifugation, the black solid products were dried under vacuum at 60 ℃ overnight to obtain the YNC. The preparation process of the NC without Y SAs was similar with that of the YNC except for the use of the ZIF-8 as the pyrolysis precursor. The ScNC and LaNC were prepared using the similar method except for the use of the $Sc(acac)_3$@ZIF-8 and $La(acac)_3$@ZIF-8 instead of the $Y(acac)_3$@ZIF-8 as the pyrolysis precursors, respectively.

4. Synthesis of Ru-YNC and Ru-NC

To synthesize the Ru-YNC, 25 mg $RuCl_3$ $3H_2O$ was firstly dissolved in 50 mL of deionized water to prepare 0.5 mg mL^{-1} impregnation solution. Afterward, 50 mg YNC was added to the above solution under magnetic stirring at room temperature. After stirring for another 6 h, the black powders were collected by centrifugation and washed with ethanol for three times, followed drying under vacuum at 60 ℃ overnight. Then the powders were placed in a tube furnace and reduced at 300 ℃ for 2 h in 5% H_2/Ar atmosphere with a heating rate of 2 ℃ min^{-1} to obtain the Ru-YNC. The preparation process of the Ru-YNC-*x* (*x* = 0. 25 and 0.75, where *x* represented the $RuCl_3$ solution concentration, mg mL^{-1}) was similar with the Ru-YNC except for the use of 0.25 and 0.75 mg mL^{-1} impregnation solution. The Ru-NC without Y single atoms was synthesized using the similar method except for the use of the NC instead

of the YNC as support. The Ru-ScNC and Ru-LaNC were prepared using the similar method except for the use of the ScNC and LaNC instead of the YNC as supports, respectively.

5. Synthesis of NiFe-LDH@NF

Before the experiment, nickel foam was firstly washed with acetone, 6 M HCl aqueous solution, ethanol, and deionized water under sonication treatment for each 20 min to clean the surface. Then, 1 mmol (0.291 g) $Ni(NO_3)_2 \cdot 6H_2O$, 0.6 mmol (0.242 g) $Fe(NO_3)_3 \cdot 9H_2O$, 2 mmol (0.074 g) NH_4F, and 5 mmol (3 g) $(NH_2)_2CO$ were dissolved in 20 mL of deionized water under stirring to obtain a transparent solution. The resultant solution together with a piece of pre-treated nickel foam (2×3 cm^2) were transferred into a 30 mL Teflon-lined stainless-steel autoclave for hydrothermal reaction at 120 ℃ for 6 h. After cooling down to room temperature, the sample was washed with ethanol, followed drying under vacuum at 60 ℃ overnight to obtain the NiFe-LDH deposited on nickel foam (NiFe-LDH@NF).

6. Characterizations

Scanning electron microscopy (SEM) was carried out on a Hitachi FE-S4800 microscope. Transmission electron microscopy (TEM) and high-angle annular dark-field scanning transmission electron microscopy (HAADF-STEM) were performed by a FEI Tecnai F30 microscope at 300 kV. Aberration-corrected high-angle annular dark-field scanning transmission electron microscopy (AC-HAADF-STEM) and corresponding energy dispersive X-ray (EDX) elemental mapping were recorded on a Thermo Fisher Themis Z microscope operated at 300 kV. Powder X-ray diffraction (XRD) was obtained on a PANalytical X'Pert Pro X-ray diffractometer with Cu Kα (λ = 1.5406 Å) radiation. X-ray photoelectron spectroscopy (XPS) was performed on an AXIS Supra X-ray photoelectron spectrometer. Element contents were determined by a Prodigy 7 inductively coupled plasma atomic emission spectrometer (ICP-AES). All the catalyst samples were digested by microwave digestion. Specifically, 50 mg catalyst powder was dissolved

in 5 mL of aqua regia (V_{HCl}:V_{HNO_3} = 3:1), then the prepared solution was digested in a microwave digestion tank at 150 ℃ for 20 mins and held at 220 ℃ for 40 mins with a heating rate of 5 ℃ min^{-1}. The collected digestion solution was diluted to 50 mL for subsequent ICP-AES analysis. N_2 adsorption-desorption isotherms were measured on a Micromeritics ASAP2460 instrument and after the samples were degassed about 4 h at 100 °C and the specific surface areas were calculated by the Brunauer-Emmett-Teller (BET) method. Electrochemical *in situ* Raman spectroscopy was obtained from a Shamrock 500i Raman spectrometer with a 532 nm laser source. The *in situ* attenuated total reflectance surface-enhanced infrared absorption spectroscopy (ATR-SEIRAS) measurements were conducted using a Nicolet Nexus 670 spectrometer equipped with a liquid nitrogen-cooled mercury-cadmium-telluride (HgCdTe) detector. X-ray absorption find structure (XAFS) data at the K-edge of Ru and Y were recorded in fluorescent mode with the large angle Lytle detector at the BL20U1 hard X-ray branch of the Energy Material Beamline in Shanghai Synchrotron Radiation Facility (SSRF). The station was operated with a Si (111) double crystal monochromator. During the measurement, the storage ring was operated at an energy of 3.5 GeV and a current of 200 mA (top-up). The photon energy was calibrated with the first inflection point in Ru K-edge of Ru foil and Y K-edge of Y foil. The ATHENA module of the IFEFFIT software packages was applied to process the acquired XAS raw data according to the standard procedures. Least-squares curve-fitting of EXAFS data was performed using an ARTEMIS program. The WT fitting parameters were set as following: *R* range: 0 to 4 Å, *k* range: 0 to 16 $Å^{-1}$, and *k* weight: 2; furthermore, a Morlet function with κ = 10, σ = 1 was used as the mother wavelet to provide the overall distribution.

7. Electrochemical measurements

The electrochemical measurements were conducted in a standard three-electrode setup on a CHI 760E electrochemical workstation (Chenhua Instruments, Shanghai, China). The graphite rod was utilized as the counter electrode, and the Hg/HgO (filled

in 1.0 M KOH) was utilized as the reference electrode. To prepare the working electrode, 5 mg catalysts and 20 μL of Nafion D521 solution were dispersed in a mixed solvent containing 480 μL of deionized water and 500 μL of isopropanol, and then ultrasonicated for at least 30 min to form a homogeneous catalyst ink. Afterward, a certain volume of the catalyst ink was dropped onto a clean hydrophilic carbon paper and dried in air. The catalyst loading amount was determined as 0.5 mg cm^{-2}. All the recorded potentials were referenced to the reversible hydrogen electrode (RHE): $E_{RHE} = E_{Hg/HgO} + 0.098 + 0.059 \times pH$. The HER measurements were performed in a N_2-saturated 1 M KOH solution. The effective geometric surface area of the hydrophilic carbon paper electrodes that were used in measurements in the three-electrode setup was 0.5×1 cm^2. Before measurements, multiple cyclic voltammetry (CV) scans were performed till a stable state of the electrodes was reached. The polarization curves were obtained at a scan rate of 5 mV s^{-1} with 95% *iR*-correction. The Tafel slopes of the catalysts were obtained by logarithmic data processing of the polarization curves. Accelerated durability tests were performed by cycling between 0 to -0.2 V *vs.* RHE for 10000 CV cycles at a scan rate of 50 mV s^{-1}. Electrochemical impedance spectroscopy (EIS) measurements were carried out at -0.1 V *vs.* RHE over a frequency range from 100 kHz to 0.1 Hz with an amplitude of 10 mV. The stability of the catalysts was evaluated by means of chronopotentiometry at the constant cathodic current density of 10 mA cm^{-2}.

8. Calculation method of electrochemical surface area

The CV test was carried out in 1.0 M KOH to evaluate the electrochemical double-layer capacitance (C_{dl}), which can further estimate the effective electrode surface areas (ECSA) of the catalysts. In detail, a series of CV tests were performed at scan rates of 20, 40, 60, 80 and 100 mV s^{-1} in the potential window of 0.10-0.20 V *vs.* the Hg/HgO electrode and the number of cycles was set to 10 to ensure consistency. By plotting the difference in current density (J) between the anodic and cathodic sweeps (J_{anodic} - $J_{cathodic}$) at 0.15 V *vs.* Hg/HgO against the scan rate, a linear trend was

observed. The slope of the fitting line was found to be equal to twice the C_{dl}, which was proportional to the effective electrode surface area of the materials. Therefore, the electrochemical surface areas of different samples can be compared with one another based on their C_{dl} values. However, it should be noted that this comparison makes sense only when the measurement of materials was carried out under the same condition.

The ECSA value was calculated from the C_{dl} value using the following equation:

$$\text{ECSA}=\frac{C_{dl}}{60\ \mu\text{F cm}^{-2}\ \text{per cm}^2_{\text{ECSA}}} \quad \text{(S1)}$$

9. Calculation method of turnover frequency

The turnover frequency (TOF, s^{-1}) per metal site was calculated according to the following equation:

$$\text{TOF} = \frac{j}{n \times F \times N} \quad \text{(S2)}$$

where j is the geometric current density, n is the number of electrons transferred in the reactions (2 for HER), F is the Faraday constant (96485 C mol^{-1}), N is the molar number of active sites. Considering that Ru clusters serve as the predominant active sites in the integrated Ru-YNC catalyst, only Ru sites in the Ru-YNC, Ru-NC, and Ru/C_{com} were considered for calculating the corresponding TOF values, while only Pt sites in the Pt/C_{com} were considered. Specifically, N was estimated *via* the total catalyst mass loading on the electrode (m, mg cm^{-2}), the weight percent of active metals in the catalysts (w, wt.%), and the molar mass (M, g mol^{-1}) according to the following equation:

$$N = \frac{m \times w}{M} \quad \text{(S3)}$$

10. CO-stripping experiments

The CO-stripping experiments were carried out in 1.0 M KOH solution using a standard three-electrode system where Hg/HgO electrode was used as the reference electrode, and Pt wire served as the counter electrode. To prepare the working electrode, 4 mg catalyst was firstly ultrasonically dispersed in 1050 μL of mixed

solvent containing 250 μL of deionized water, 750 μL of ethanol and 50 μL of Nafion D521 solution. Afterward, 5 μL of homogeneous ink was loaded onto a glassy carbon electrode (diameter of 3 mm, effective area of 0.1971 cm^2) with a total catalyst loading of 96.65 μg cm^{-2}. Before the test, high-purity Ar was bubbled for at least 30 min to remove the dissolved oxygen. The CO gas (40 vol.%) was firstly bubbled into the solution for 15 min at a potential of 0 V *vs.* RHE to ensure adequate adsorption of CO on the surface of the catalyst. Subsequently, the electrode was quickly transferred to a fresh 1.0 M KOH solution purged with high-purity Ar. The data were acquired by the CV measurement performed in the potential range from 0 to 1.2 V *vs.* RHE with a scan rate of 50 mV s^{-1} at room temperature.

11. Metal center poisoning experiments

The metal center poisoning experiments were implemented using thiocyanate ions (SCN^-) as deactivator, which were conducted by carrying out chronoamperometry test for the Ru-YNC and YNC in 20 mL of 1.0 M KOH solution. The constant potentials applied to the Ru-YNC and YNC were -0.07 and -0.7 V *vs.* RHE, respectively. After about 830 s of running, 10 mL of 1.0 M KOH solution containing 15 mmol KSCN was rapidly added. The subsequent current changes were recorded.

12. Electrochemical *in situ* Raman measurements

The hardware of *in situ* Raman measurements mainly consists of five parts: a spectrometer (Shamrock 500i), a laser controller, a Leica microscope (DM2700M ICC50W), a displacement table (MARZHAUSER SCANplus75×50), and a Raman excitation box. All the spectra were obtained at room temperature with excitation at 532 nm. Calibration was performed using the 520 cm^{-1} peak (silicon wafer standard). Electrochemical *in situ* Raman measurements were performed on a homemade electrochemical reaction cell using a standard three-electrode system in 1.0 M KOH electrolyte. Specifically, Hg/HgO electrode was used as the reference electrode, Pt wire served as the counter electrode. To prepare the working electrode, 5 mg catalyst was firstly ultrasonically dispersed in 1 mL of mixed solvent containing 480 μL of

deionized water, 500 μL of isopropanol and 20 μL of Nafion D521 solution. Afterward, 50 μL of homogeneous ink was loaded onto a piece of hydrophilic carbon paper with an area of 1 cm^2, ensuring the total catalyst loading of 0.25 mg cm^{-2}. The electrochemical *in situ* Raman data were acquired from the chronoamperometry measurements performed in the potential range from 0 to -0.2 V *vs.* RHE.

13. Electrochemical *in situ* ATR-SEIRAS measurements

The electrochemical *in situ* ATR-SEIRAS measurements were conducted using a Nicolet Nexus 670 spectrometer equipped with a liquid nitrogen-cooled mercury-cadmium-telluride (HgCdTe) detector. To enhance the signal intensity, a gold layer was deposited onto the surface of the monocrystalline silicon substrate. Then, 20 μL of uniform ink (prepared by ultrasonic dispersion of 5 mg of catalyst in 1000 μL of solvent, consisting of 480 μL water, 500 μL isopropanol, and 20 μL naphthol solution) was dropped onto the gold film surface and used as the working electrode. A platinum sheet and an Hg/HgO electrode were used as the counter and reference electrodes, respectively. The electrochemical *in situ* ATR-SEIRAS measurements were performed using LSV scanning within a potential range of 0 to -0.4 V *vs.* RHE at a scan rate of 10 mV s^{-1}.

14. Anion-exchange-membrane water electrolysis electrolyzer

The anion-exchange-membrane water electrolysis (AEMWE) electrolyzer with a serpentine flow channel and an effective area of 2×2 cm^2 was used to evaluate the application prospect of the Ru-YNC in the practical water electrolysis. The Ru-YNC, commercial Pt/C (Pt/C_{com}) and Ru/C (Ru/C_{com}) were employed as cathodic catalysts, while the prepared NiFe-LDH@NF was used as anodic catalyst. The anion exchange membrane was immersed into 1.0 M KOH solution for at least 24 h prior to being used to exchange Cl^- into OH^-. Hydrophilic carbon paper (CP) was used as a cathode porous current collector. The Ru-YNC, Pt/C_{com} and Ru/C_{com} catalyst ink were sprayed onto the CP using an air spray gun, and the total catalyst loading amount is about 2.0 mg cm^{-2}. The corresponding noble metal loadings of the Ru-YNC, Pt/C_{com}, and

Ru/C_{com} cathodes were 0.019, 0.4, and 0.1 mg cm^{-2}, respectively. The anion exchange membrane was sandwiched between the catalyst-coated CP and NiFe-LDH@NF. All the AEMWE electrolyzers were operated at 80 ℃ with a peristaltic pump pumping 1.0 M KOH at a flow rate of 30 mL min^{-1}. Polarization curves were obtained from 1.4-2.0 V at a scan rate of 2 mV s^{-1}. The stability test of the Ru-YNC||NiFe-LDH was conducted by measuring the voltage at a current density of 500 mA cm^{-2} operated at 80 ℃ in 1.0 M KOH solution.

15. Calculations of AEMWE electrolyzer efficiency and H_2 cost

The calculations were carried out strictly in accordance with the method proposed in the previous reports,[1,2] with sole consideration given to the electricity costs. As an illustrative case, the calculation of the AEMWE electrolyzer efficiency at a current density of 0.5 A cm^{-2}, where the Ru-YNC was used as the cathode and the homemade NiFe-LDH as the anode, is presented as follows:

(1) H_2 production rate @ 0.5 A cm^{-2}

= (j A cm^{-2})(1 e^- / 1.602 $\times 10^{-19}$ C)(1 H_2 / 2 e^-)

= 0.5 A cm^{-2} / (1.602 $\times 10^{-19}$ C $\times 2$) = 2.59 $\times 10^{-6}$ mol H_2 cm^{-2} s^{-1}

(2) Lower heating value (LHV) of H_2

= 120 kJ g^{-1} H_2 = 2.42 $\times 10^5$ J mol^{-1} H_2

(3) H_2 power out

= (2.59 $\times 10^{-6}$ mol H_2 cm^{-2} s^{-1}) $\times$ (2.42 $\times 10^5$ J mol^{-1}) = 0.63 W cm^{-2}

(4) AEWME electrolyzer power @ 0.5 A cm^{-2} = (0.5 A cm^{-2}) (1.78 V) = 0.89 W cm^{-2}

(5) AEWWE electrolyzer efficiency

= (H_2 power out) / (AEWME electrolyzer power) = 0.63 W cm^{-2} / 0.89 W cm^{-2} = 70.79%

(6) Price per gasoline-gallon equivalent (GGE) H_2

= 1 GGE H_2/H_2 production rate $\times$ AEWME electrolyzer power $\times$ Electricity bill

$= 0.997\ \text{kg} / (2.59 \times 10^{-6}\ \text{mol}\ H_2\ \text{cm}^{-2}\ \text{s}^{-1} \times 2\ \text{kg/mol}) \times 0.89\ \text{W cm}^{-2} \times \$0.02 / \text{kW h}$

$= \$0.93 / \text{GGE}\ H_2$

16. Density functional theory calculations

All calculations were performed using the Vienna Ab Initio Simulation Package (VASP) with the spin-polarized density functional theory (DFT) method. The valence-core electron interactions were treated by Projector Augmented Wave (PAW) potentials and the electron exchange correlation interactions were described by the generalized gradient approximation (GGA) with the Perdew-Burke-Emzerhof (PBE) functional. Considered long-range interactions between molecules/intermediates and surface and van der Waals interactions were considered using DFT-D3 correlation. To avoid effects coming from other slabs, a vacuum of 15 Å was added along the *z* direction. The convergence criterion of geometry relaxation was set to 0.01 eV $\cdot$Å^{-1} in force on each atom. The energy cutoff for plane wave-basis was set to 500 eV (ENCUT = 500). The *K* points were sampled with $3 \times 3 \times 1$ by Monkhorst-Pack method. Moreover, The *K* points were set as $6 \times 6 \times 1$ for the electronic static calculation (density of states, electron localization function and bonding analysis), and meanwhile the energy cut-off of plane wave was increased to 700 eV. The free energies of different reaction steps were calculated as $G = E_{DFT} + E_{ZPE} - T\Delta S$, where E_{DFT} is the DFT calculated energy, E_{ZPE} and $T\Delta S$ are calculated by DFT vibration frequency calculations. In order to consider the effect of an applied electric potential on the electrode reaction, a value of $-neU$ was added to calculate the free energy of each step, where *n* is the number of electrons involved in the reaction, *U* is the applied bias.

According to the coordination numbers of the Ru-Ru (~6), Ru-N (~2), and Y-N (~4) in the EXAFS fitting data, the Ru-YNC basic model was determined to comprise the Y-N_4 sites and Ru_{13} clusters, and the Ru-NC and YNC are composed of isolated Y-N_4 sites and Ru_{13} clusters, respectively. As for the Ru-ScNC and Ru-LaNC, the corresponding models are constructed according to the combination of Ru_{13} cluster and Sc-N_4 or La-N_4 sites, respectively.

For the HER process, the hydrogen adsorption free energy (ΔG_{H^*}) was calculated by the following equation:

$$\Delta G_{H^*}=\Delta E_{H^*}+0.24\ \text{eV} \quad \text{(S4)}$$

where ΔE_{H^*} is defined by the following equation:

$$\Delta E_{H^*}=E_{H^*}-(E_*+1/2E_{H_2}) \quad \text{(S5)}$$

where E_{H^*} is the total energy of H atom on the support, E_* is the total energy of support, E_{H_2} is the energy of the gas H_2 calculated by setting the isolated H_2 in a box of 10.0 Å×10.0 Å×10.0 Å. The Gibbs free energy for the well-known highly efficient Pt catalyst is near-zero as $|\Delta G_{ads}| \approx 0.09$ eV.

Furthermore, the water adsorption energy ($\Delta E_{H_2O^*}$) was calculated by the following equation:

$$\Delta E_{H_2O^*}=E_{H_2O^*}-(E_*+E_{H_2O}) \quad \text{(S6)}$$

where $E_{H_2O^*}$ is the total energy of H_2O molecule on the support, and E_{H_2O} is the energy of H_2O.

The water dissociation energy (ΔG_{H_2O}) was calculated by the following equation:

$$\Delta G_{H_2O}=G_{(OH^*+H^*)}-G_{H_2O^*} \quad \text{(S7)}$$

where $G_{(OH^*+H^*)}$ and $G_{H_2O^*}$ are the Gibbs free energy of the (OH^*+H^*) and H_2O^* configurations, respectively.

Supplementary Figures

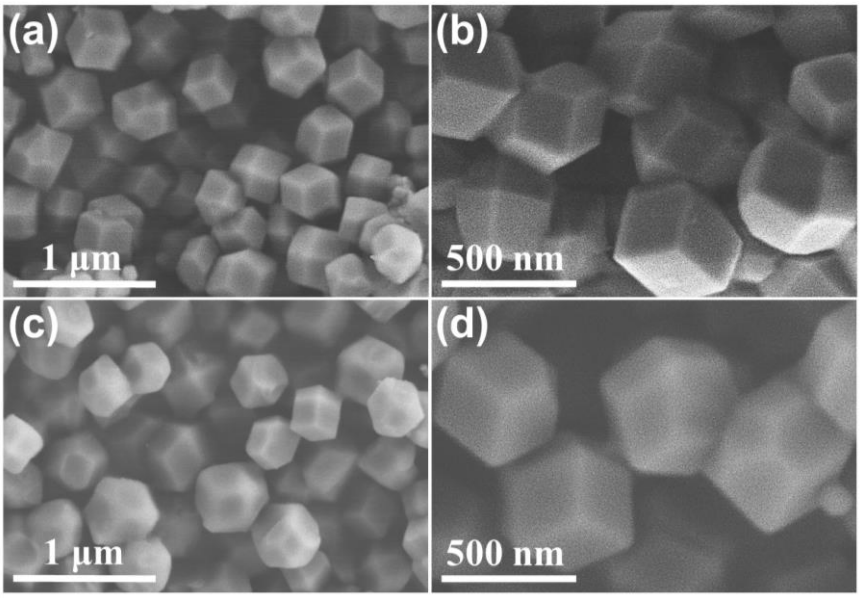

Fig. S1 SEM images of (a, b) ZIF-8 and (c, d) $Y(acac)_3$@ZIF-8.

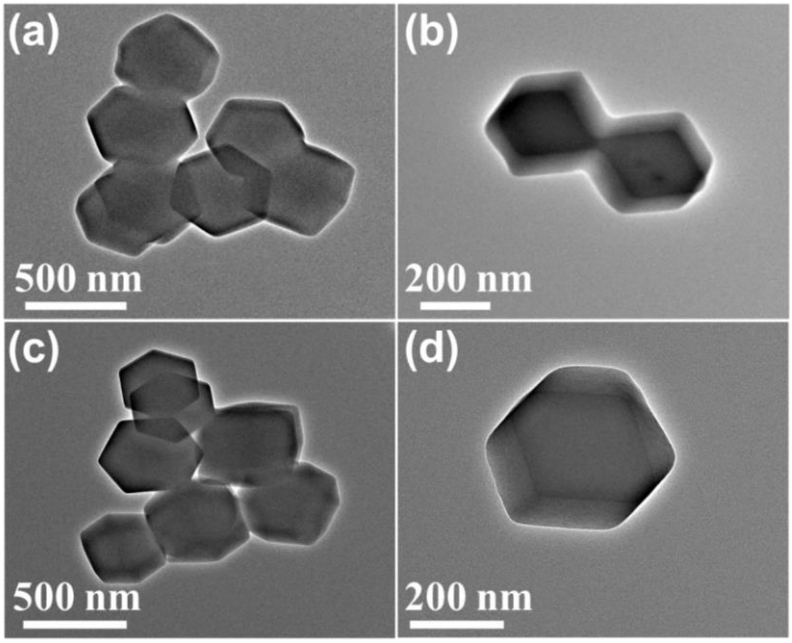

Fig. S2 TEM images of (a, b) ZIF-8 and (c, d) $Y(acac)_3$@ZIF-8.

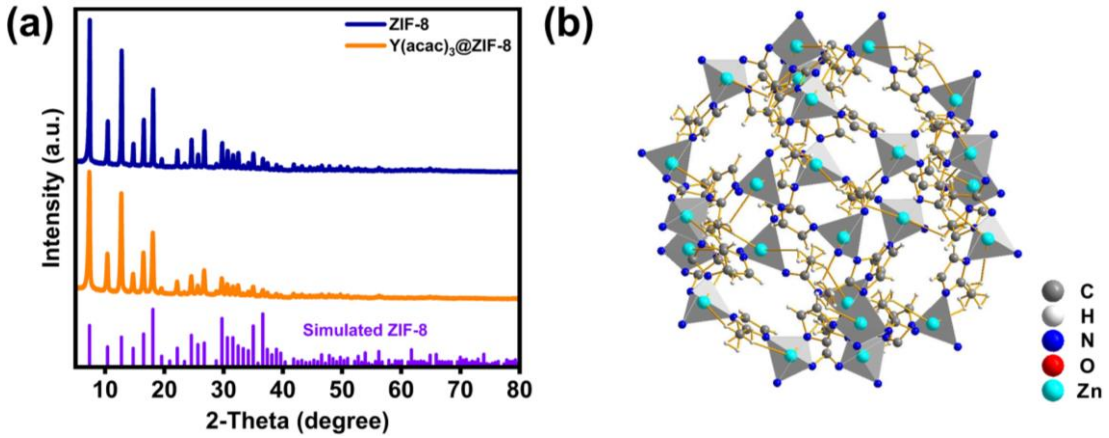

Fig. S3 (a) XRD patterns of ZIF-8 and $Y(acac)_3$@ZIF-8. (b) Simulated crystal structure of ZIF-8 using the Diamond crystallography software. Both the synthesized ZIF-8 and $Y(acac)_3$@ZIF-8 are consistent with the crystal structure of the simulated ZIF-8.

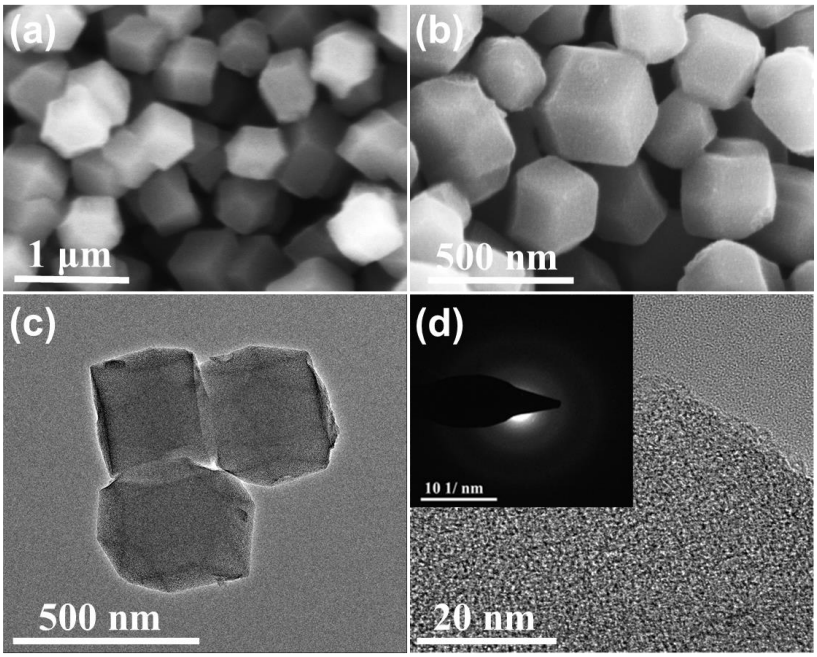

Fig. S4 (a, b) SEM and (c, d) TEM images of YNC. Inset in (d) shows the corresponding SAED pattern, which indicates the absence of Y-related crystal phase.

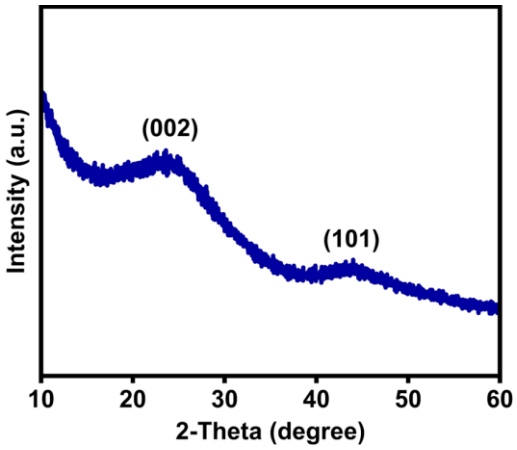

Fig. S5 XRD pattern of YNC. The two broad peaks located at about 26 ° and 44 ° are assigned to the (002) and (101) planes of graphite carbon (PDF#75-1621), respectively.

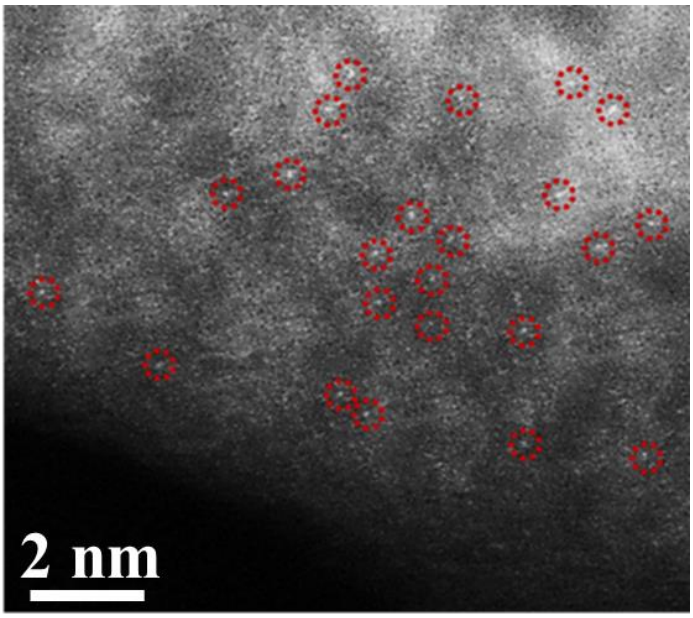

Fig. S6 AC-HAADF-STEM image of YNC. The dispersed bright dots labeled with red circles can be identified as the isolated Y SAs onto a N-doped carbon support.

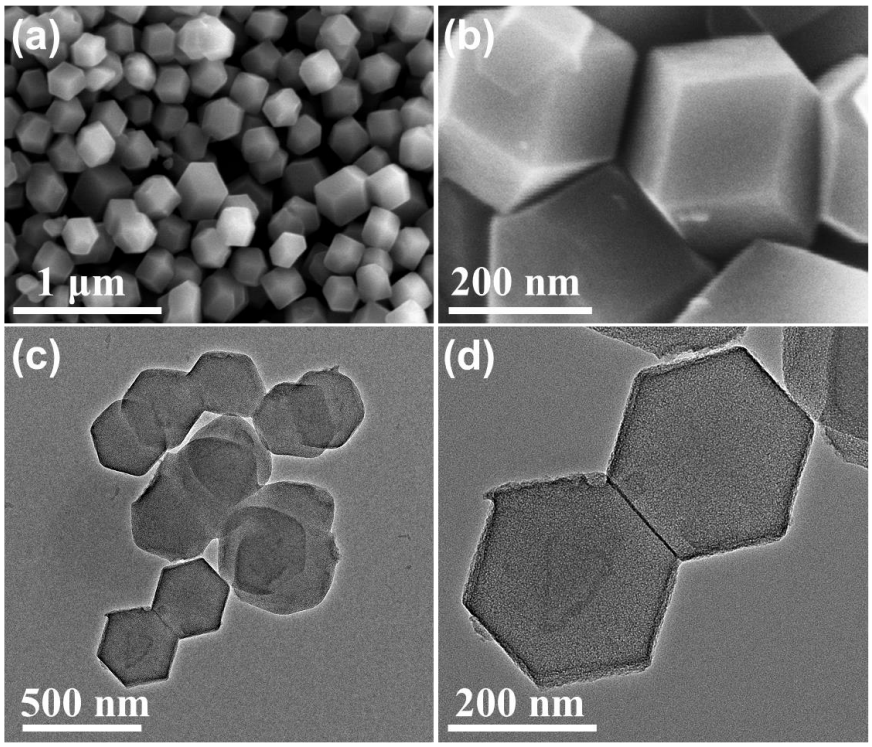

Fig. S7 (a, b) SEM and (c, d) TEM images of Ru-YNC.

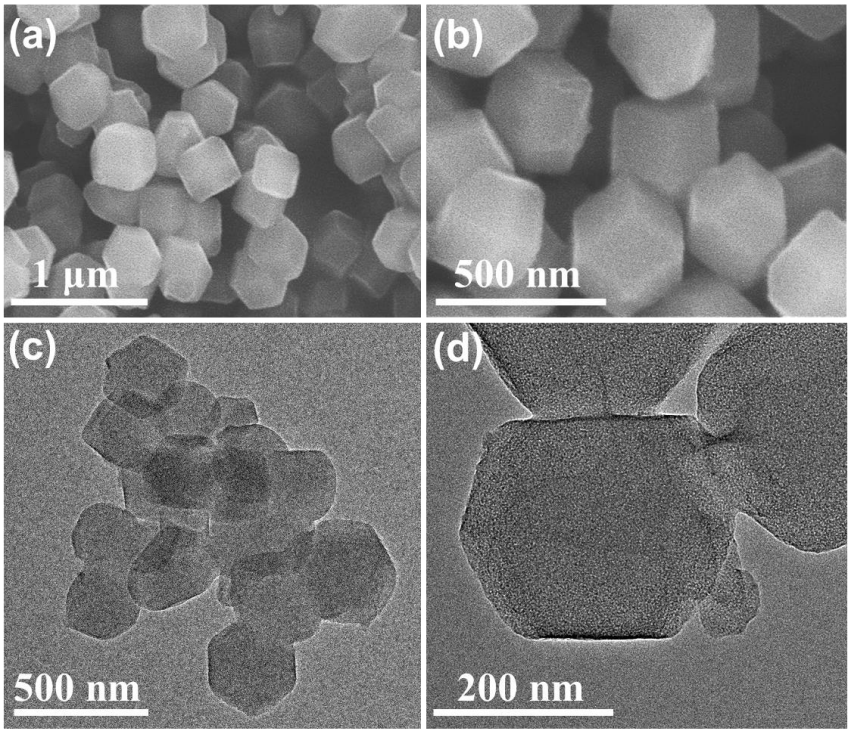

Fig. S8 (a, b) SEM and (c, d) TEM images of Ru-NC.

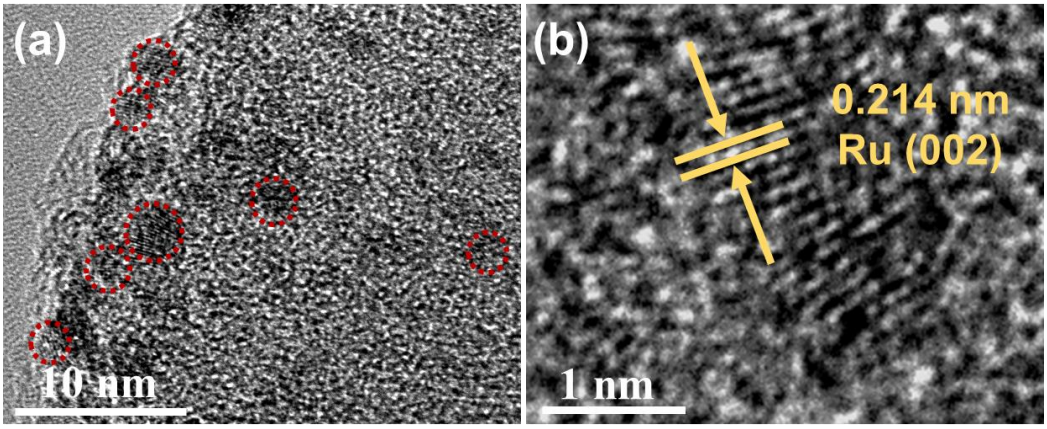

Fig. S9 (a, b) HRTEM images of Ru-YNC at different magnifications. The dispersed Ru clusters with distinct lattice fringes are marked by red circles in (a). The lattice fringes with a spacing of 0.214 nm in (b) can be assigned to the (002) plane of hexagonal close-packed (hcp) Ru (PDF#06-0663).

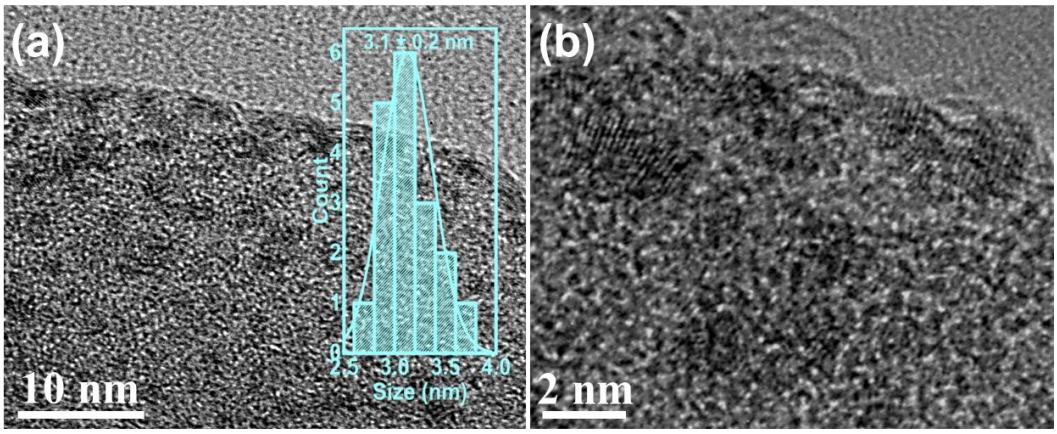

Fig. S10 (a, b) HRTEM images of Ru-NC at different magnifications. Inset in (a) shows the particle size distribution of individual Ru clusters.

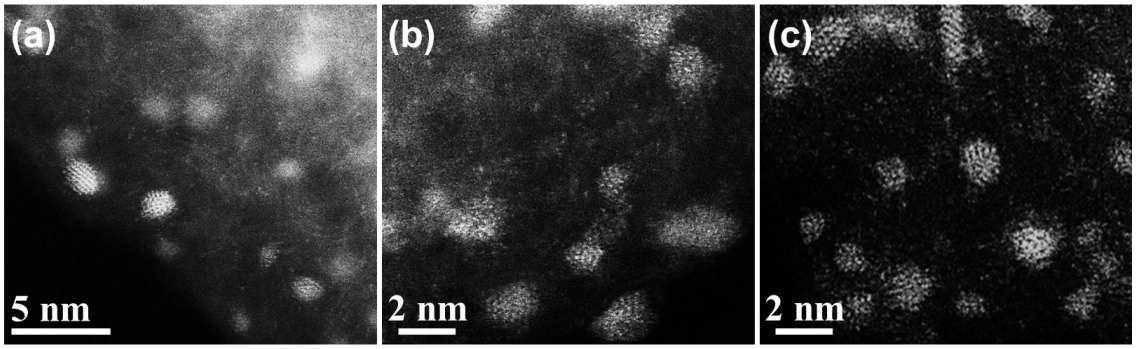

Fig. S11 (a-c) AC-HAADF-STEM images of Ru-YNC.

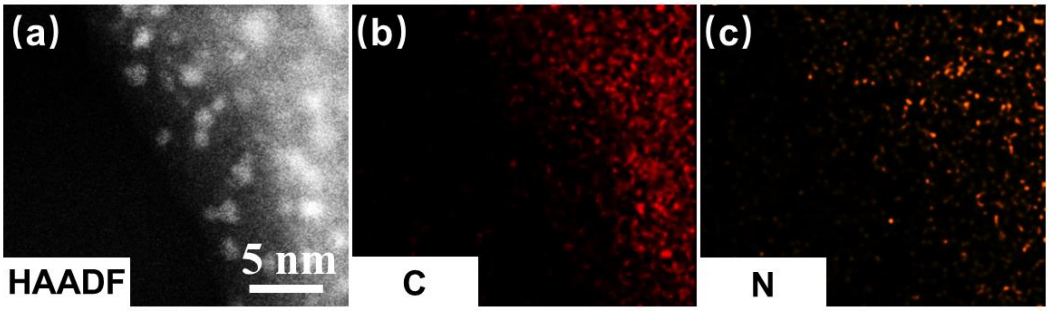

Fig. S12 (a) AC-HAADF-STEM image and corresponding elemental mapping results of (b) C and (c) N signals of Ru-YNC.

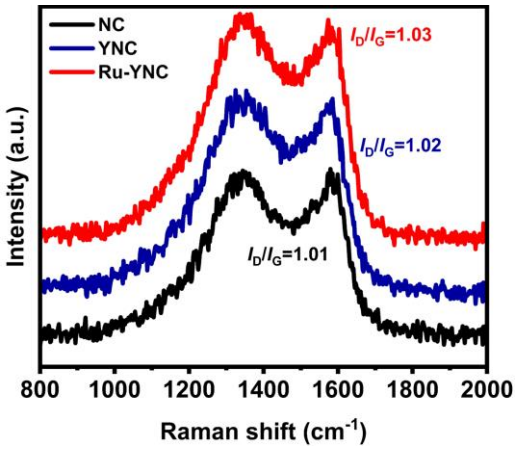

Fig. S13 Raman spectra of NC, YNC, and Ru-YNC.

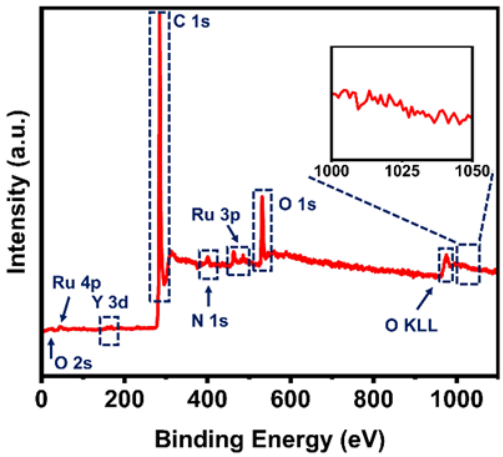

Fig. S14 XPS survey spectrum of Ru-YNC.

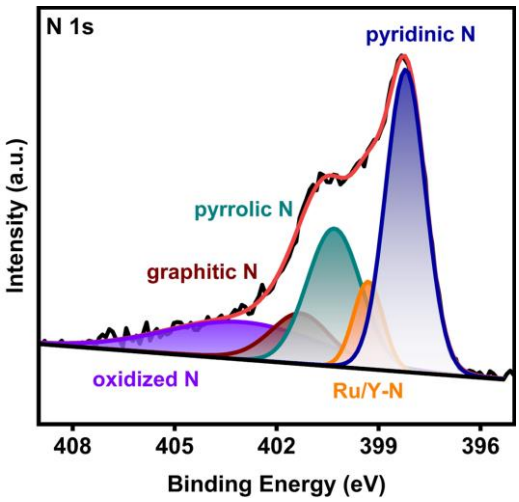

Fig. S15 High-resolution N 1s XPS spectrum of Ru-YNC.

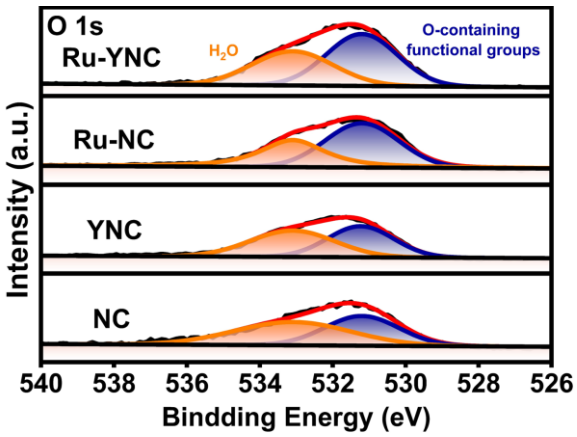

Fig. S16 High-resolution O 1s XPS spectra of Ru-YNC, Ru-NC, YNC, and NC.

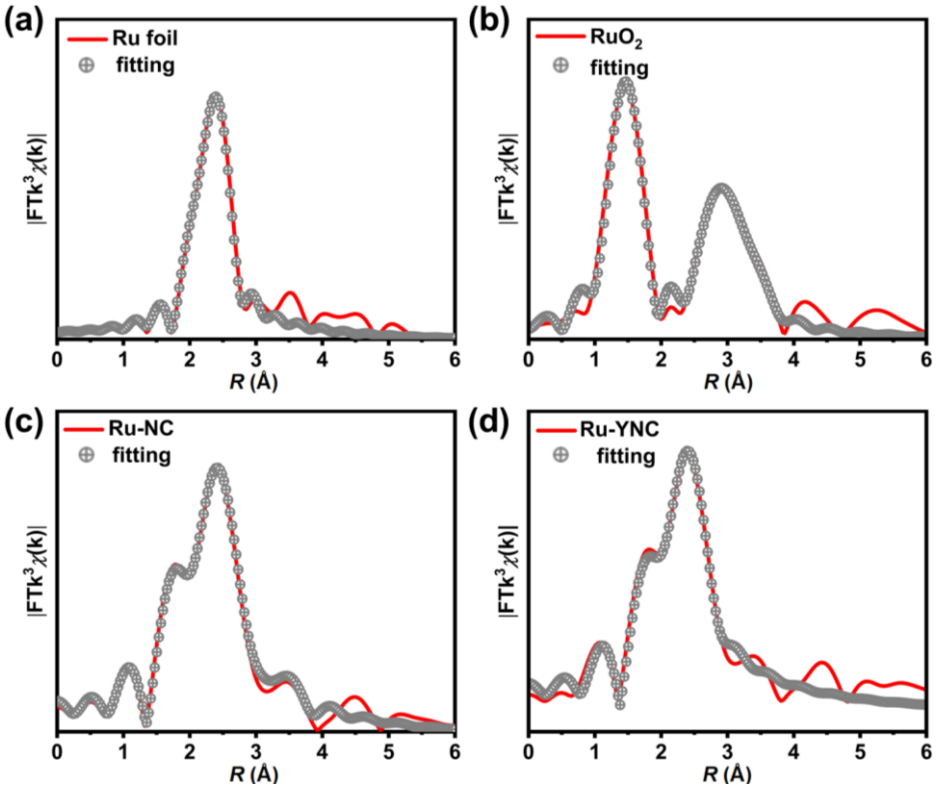

Fig. S17 Ru-K edge EXAFS experimental and fitting results of (a) Ru foil, (b) RuO_2, (c) Ru-NC, and (d) Ru-YNC in *R* space.

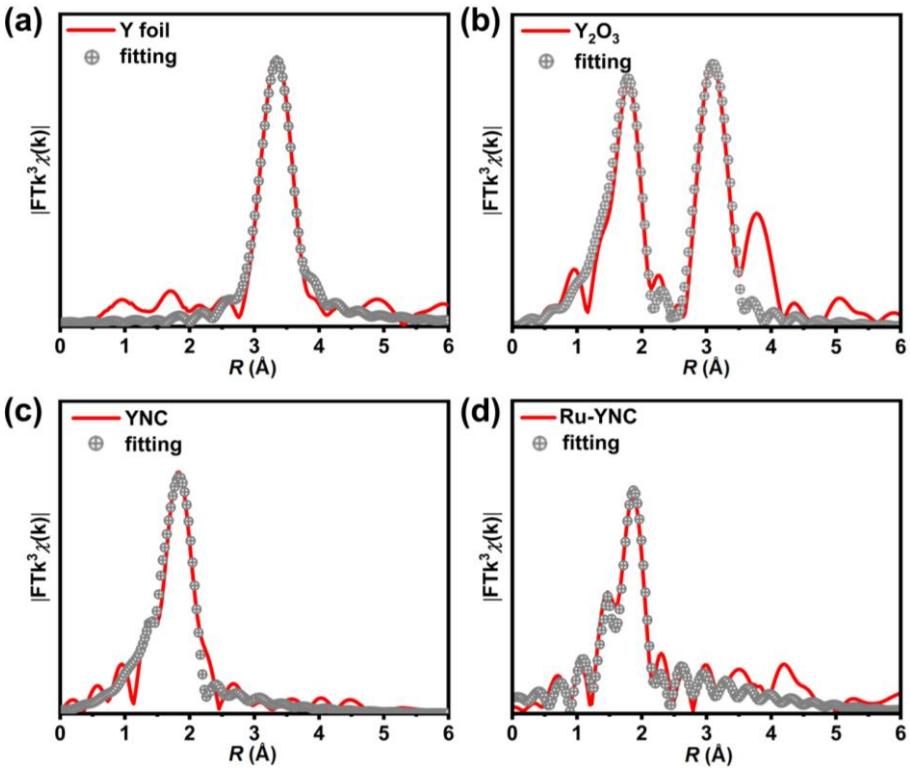

Fig. S18 Y-K edge EXAFS experimental and fitting results of (a) Y foil, (b) Y_2O_3, (c) YNC, and (d) Ru-YNC in *R* space.

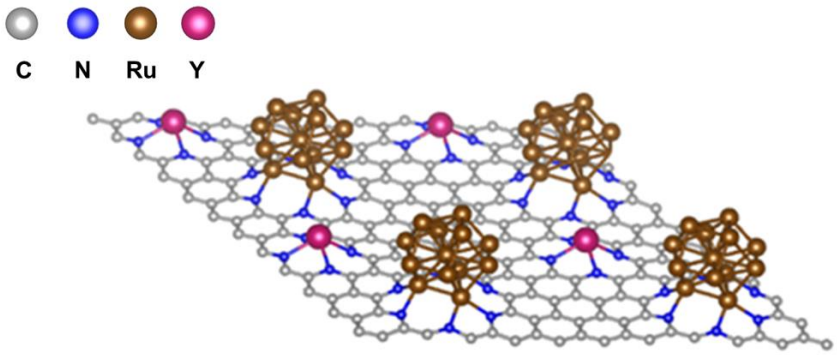

Fig. S19 Optimized local coordination configuration of Ru-YNC. According to the EXAFS quantitative fitting results, the coordination configuration of the Ru-YNC is ultimately identified to be the planar Y-N_4 moiety combined with the Ru-N_2 moiety, where the Ru clusters and Y SAs are immobilized onto a N-doped carbon support through Y-N and Ru-N bonds, respectively.

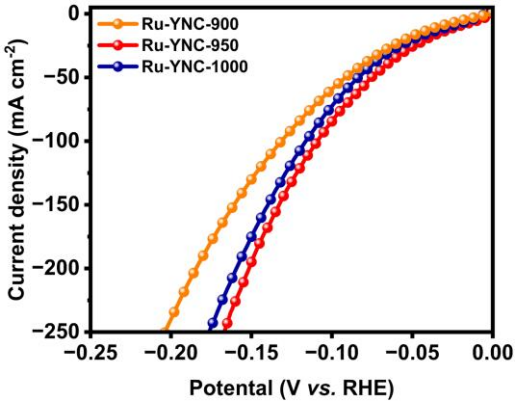

Fig. S20 LSV curves of YNC-*x* in N_2-saturated 1.0 M KOH solution (*x* = 900, 950 and 1000, where *x* represents the pyrolysis temperature, ℃).

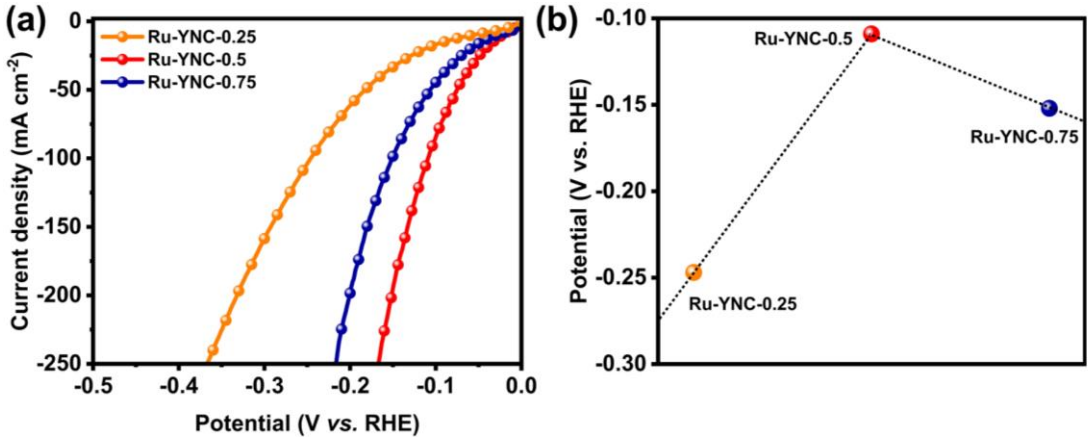

Fig. S21 (a) LSV curves of Ru-YNC-*x* in 1.0 M KOH solution (*x* = 0. 25, 0.5 and 0.75, where *x* represents the concentration of $RuCl_3$ aqueous solution during the synthesis of Ru YNC, mg mL^{-1}). (b) A volcano-type relationship between the concentration of $RuCl_3$ aqueous solution and overpotential of Ru-YNC-*x* at a current density of 100 mA cm^{-2}.

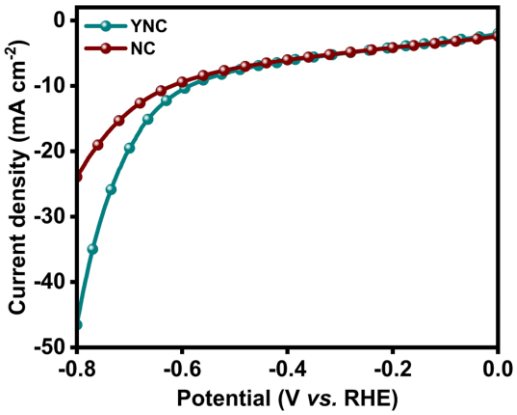

Fig. S22 LSV curves of YNC and NC in 1.0 M KOH solution. Both the YNC and NC have almost no electrochemical alkaline HER performance, which require the large overpotentials of 586 and 620 mV at a current density of 10 mA cm^{-2}, respectively.

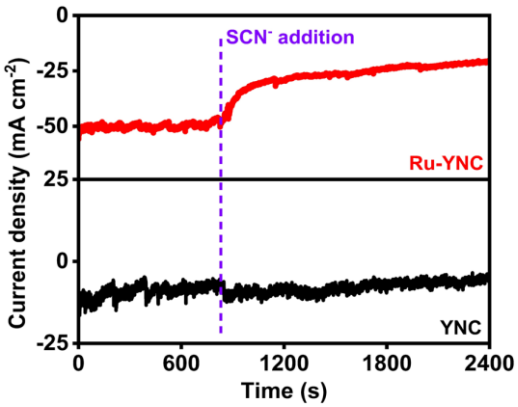

Fig. S23 Amperometric *i-t* curves of Ru-YNC and YNC in 1.0 M KOH solution with SCN^- addition. The constant potentials applied to Ru-YNC and YNC were -0.07 and -0.7 V *vs.* RHE, respectively.

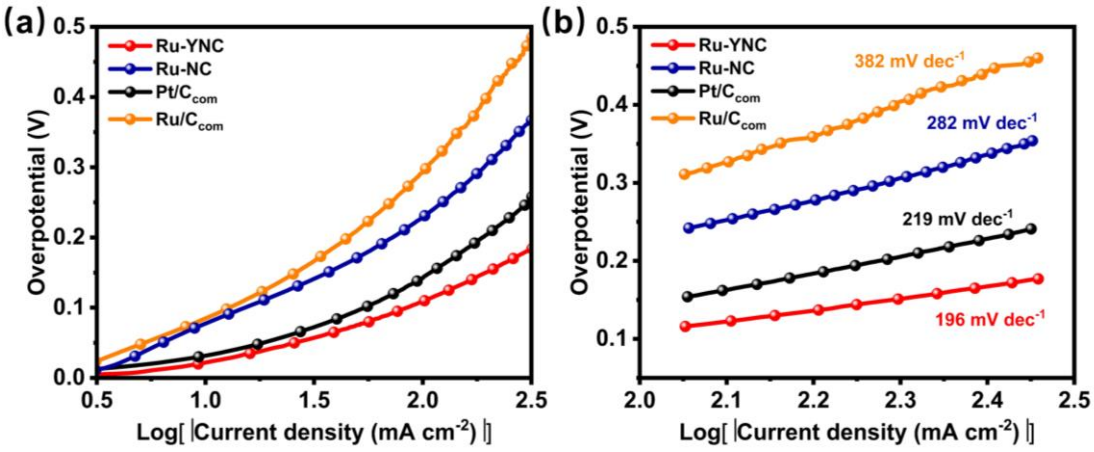

Fig. S24 (a) Full Tafel curves of the Ru-YNC and control catalysts in the HER region. (b) Tafel plots of Ru-YNC and control catalysts under high current densities.

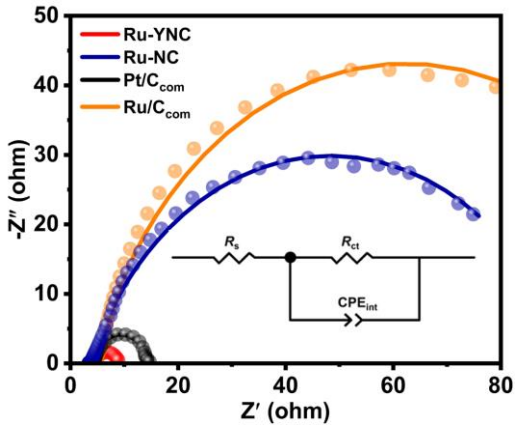

Fig. S25 Nyquist plots of Ru-YNC and control catalysts, recorded in 1.0 M KOH solution at a potential of -0.1 V *vs.* RHE. Inset is equivalent circuit for the fitting analysis of Nyquist plots. The R_s is solution resistance, the R_{ct} is charge transfer resistance, the CPE_{int} represents constant phase element replacing the capacitance of the interface double layer.

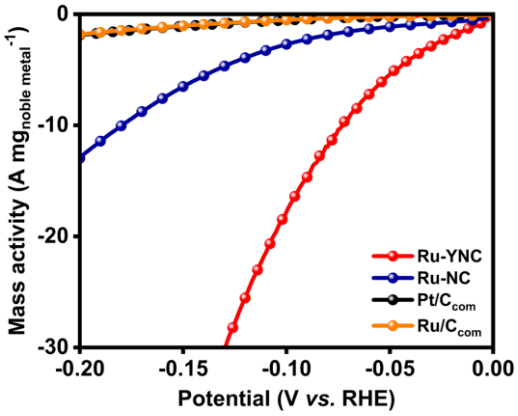

Fig. S26 LSV curves normalized by noble metal mass for Ru-YNC and control catalysts in 1.0 M KOH solution.

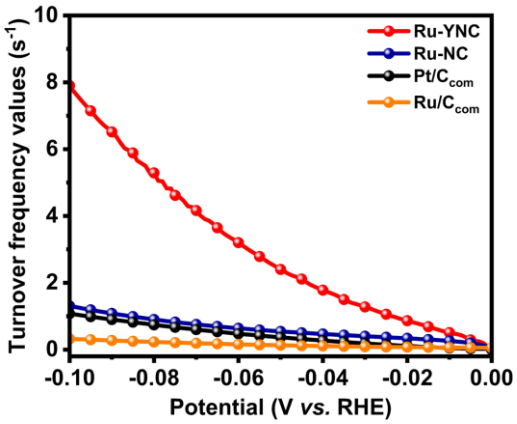

Fig. S27 Calculated TOF curves of Ru-YNC and control catalysts in 1.0 M KOH solution.

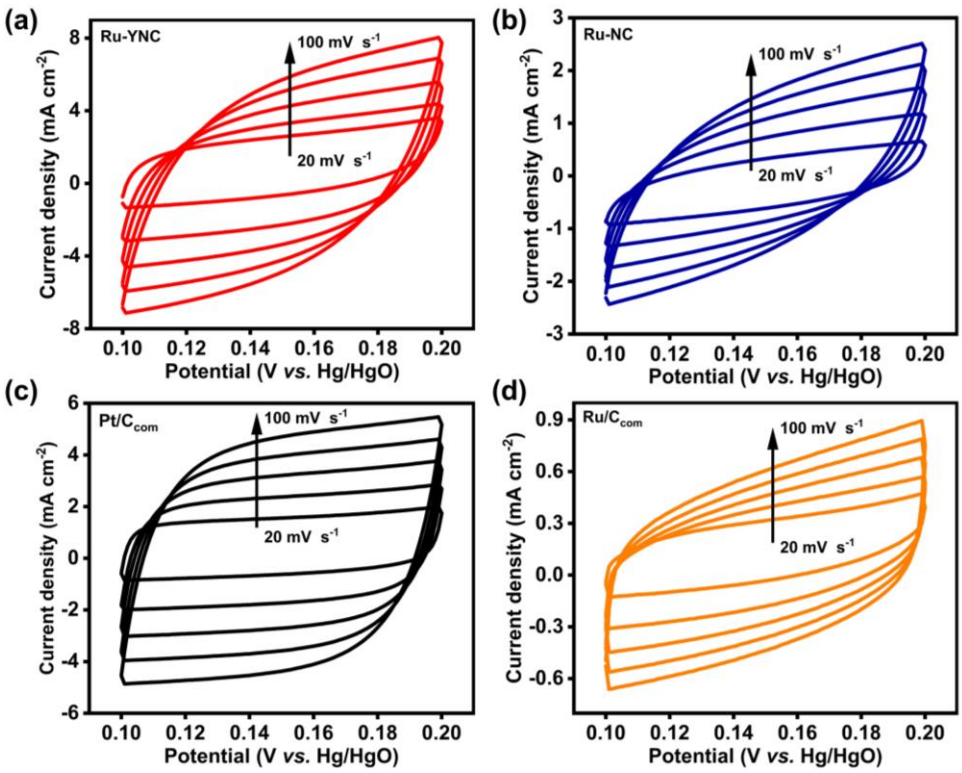

Fig. S28 CV curves of (a) Ru-YNC, (b) Ru-NC, (c) Pt/C_{com}, and (d) Ru/C_{com} in the non-Faradaic region at different scan rates in 1.0 M KOH solution.

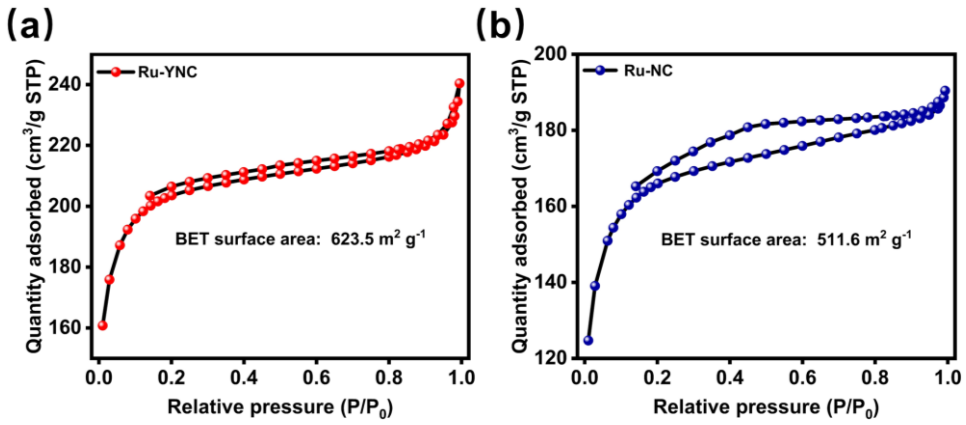

Fig. S29 N_2 adsorption-desorption isotherms of (a) Ru-YNC and (b) Ru-NC.

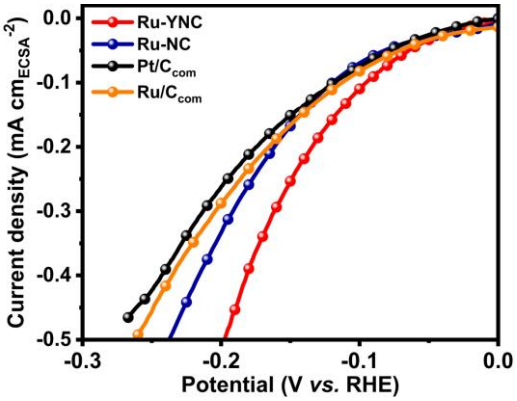

Fig. S30 LSV curves normalized by ECSA of Ru-YNC and control catalysts in 1.0 M KOH solution.

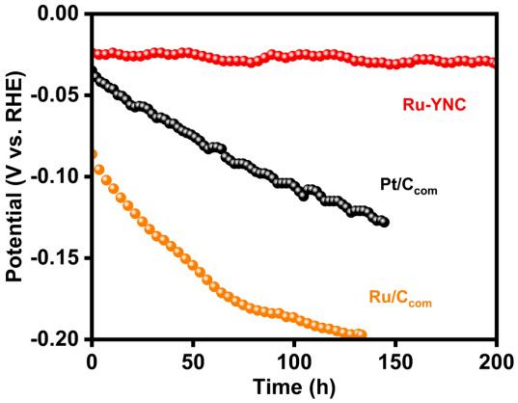

Fig. S31 Chronopotentiometry curves of Ru-YNC, Pt/C_{com}, and Ru/C_{com} at a constant current density of 10 mA cm^{-2} in 1.0 M KOH solution.

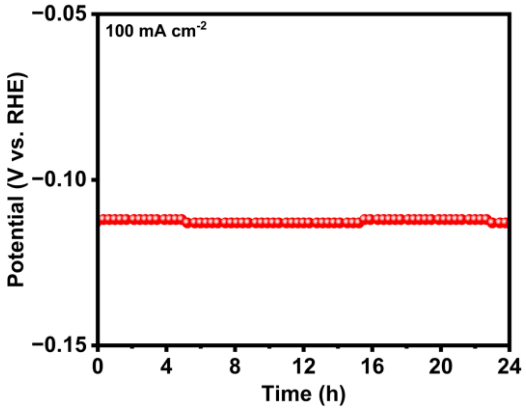

Fig. S32 Chronopotentiometry curve of Ru-YNC at a constant current density of 100 mA cm^{-2} in 1.0 M KOH solution.

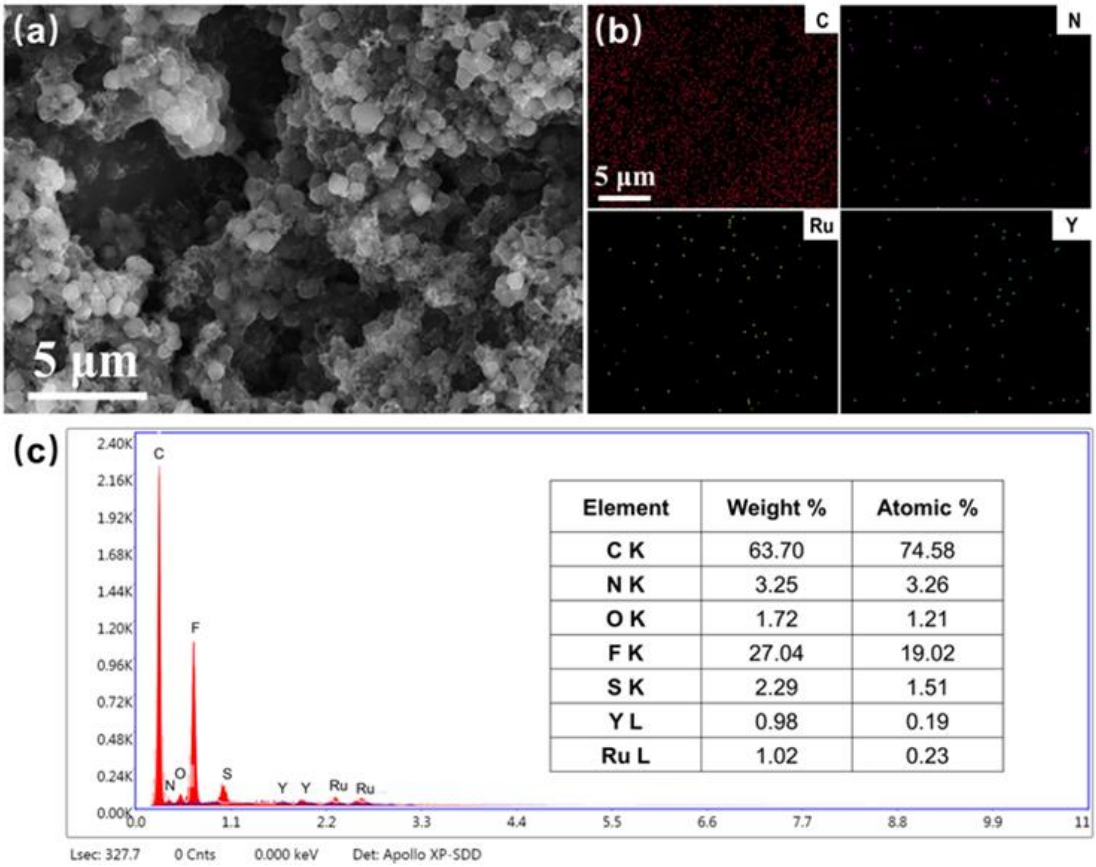

Element	Weight %	Atomic %
C K	63.70	74.58
N K	3.25	3.26
O K	1.72	1.21
F K	27.04	19.02
S K	2.29	1.51
Y L	0.98	0.19
Ru L	1.02	0.23

Fig. S33 (a) SEM image, (b) EDX elemental mapping results, and (c) EDX spectrum and elemental ratios of the initial carbon paper-supported Ru-YNC electrode.

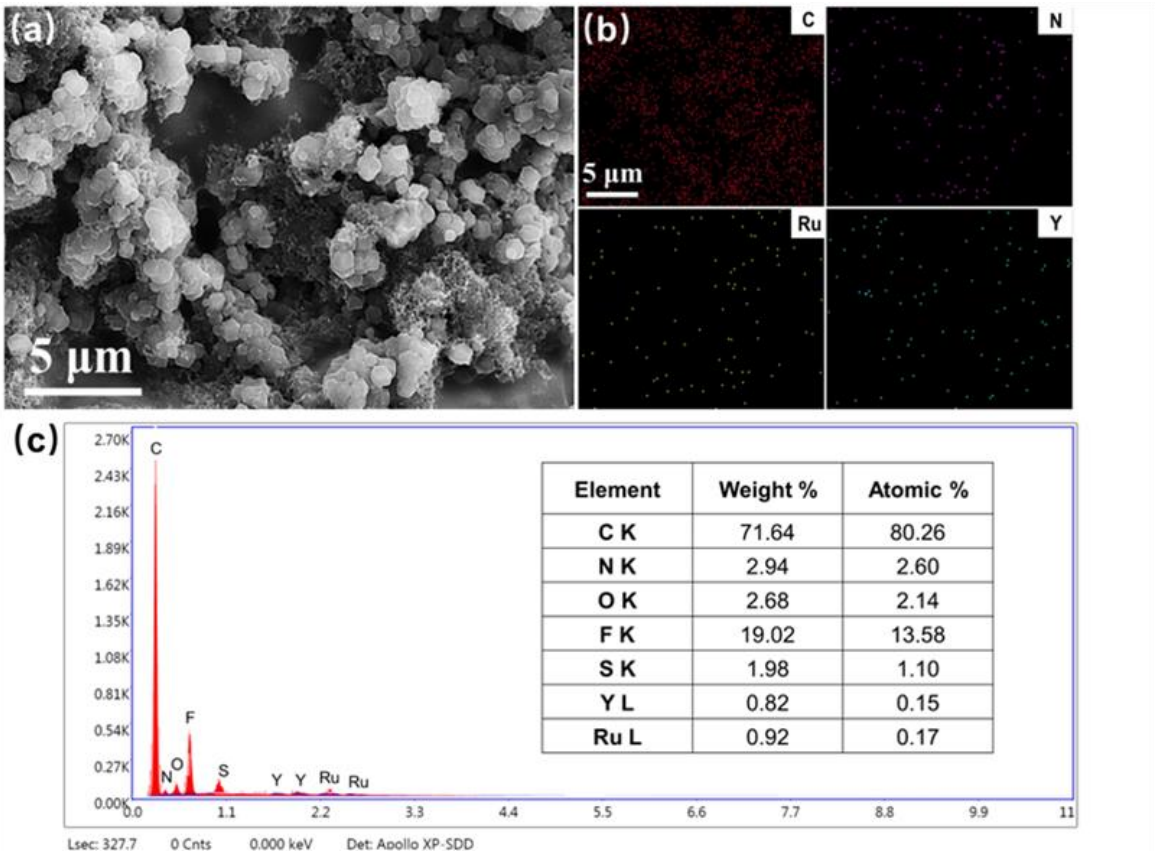

Element	Weight %	Atomic %
C K	71.64	80.26
N K	2.94	2.60
O K	2.68	2.14
F K	19.02	13.58
S K	1.98	1.10
Y L	0.82	0.15
Ru L	0.92	0.17

Fig. S34 (a) SEM image, (b) EDX elemental mapping results, and (c) EDX spectrum and elemental ratios of the carbon paper-supported Ru-YNC electrode after chronopotentiometry measurement at 100 mA cm^{-2} for 24 h.

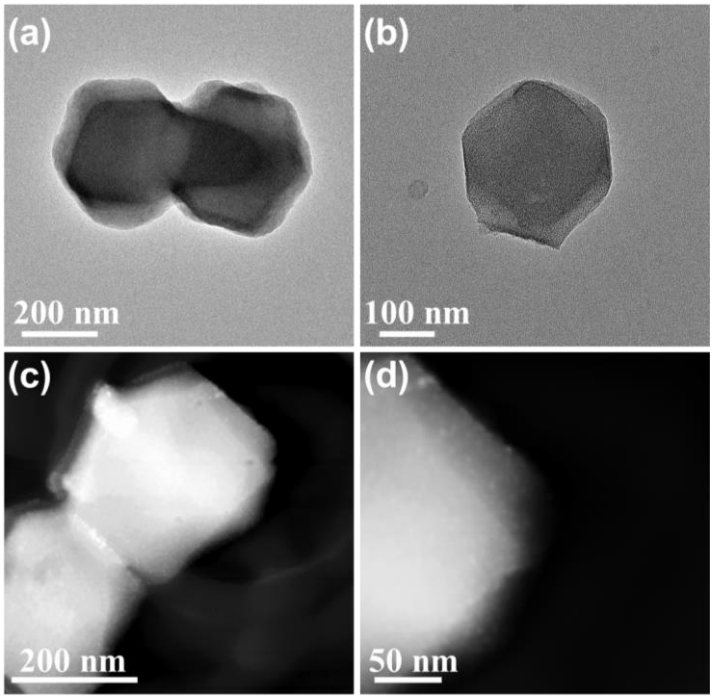

Fig. S35 (a, b) TEM and (c, d) HAADF-STEM images of Ru-YNC after chronopotentiometry measurement at 10 mA cm^{-2} for 200 h. It can be observed that the Ru-YNC still retains the rhombododecahedral morphology with well-dispersed Ru clusters after HER stability measurement.

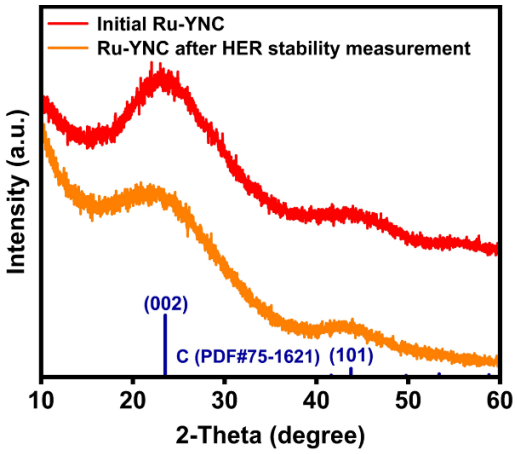

Fig. S36 XRD patterns of initial Ru-YNC and Ru-YNC after chronopotentiometry measurement at 10 mA cm^{-2} for 200 h.

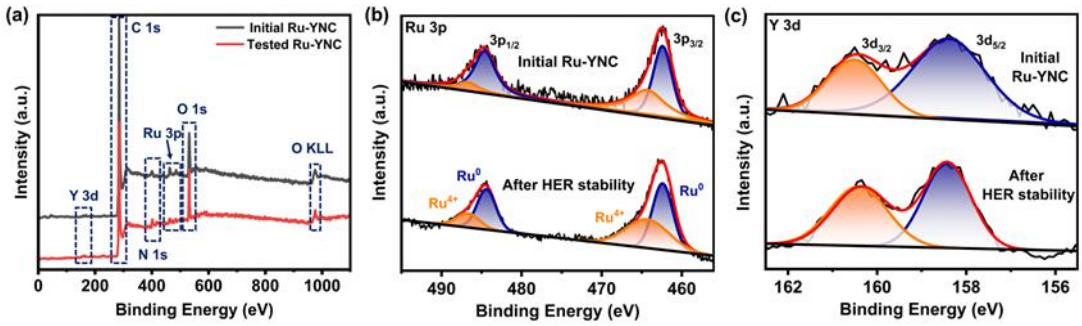

Fig. S37 XPS (a) survey, (b) high-resolution Ru 3p, and (c) high-resolution Ru Y 3d spectra of the Ru-YNC before and after chronopotentiometry measurement at 10 mA cm^{-2} for 200 h.

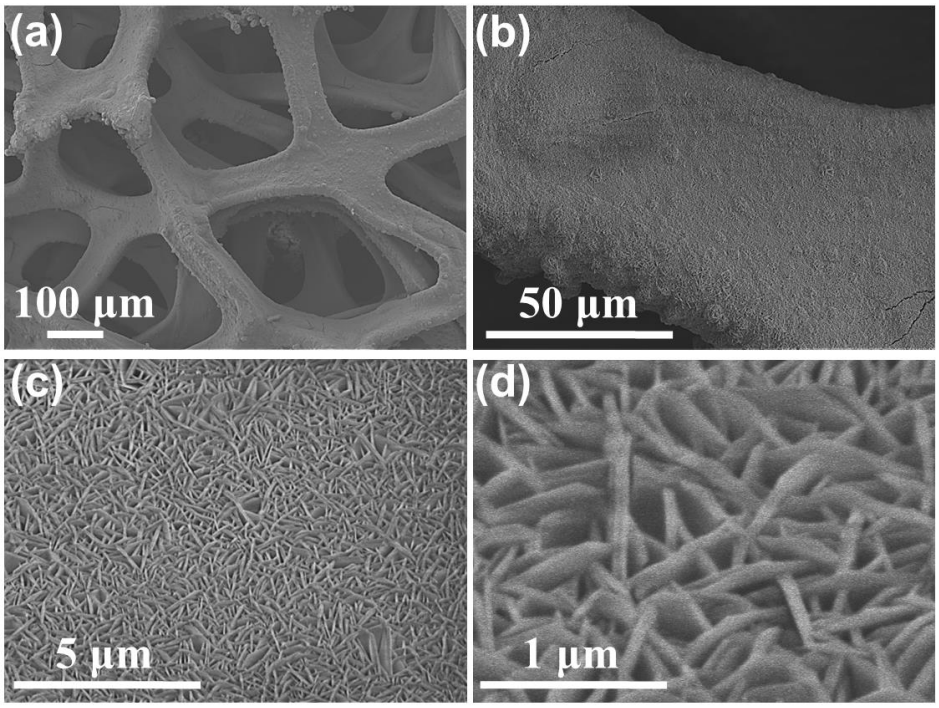

Fig. S38 (a-d) SEM images of homemade NiFe layered double hydroxide deposited on nickel foam (NiFe-LDH@NF) at different magnifications.

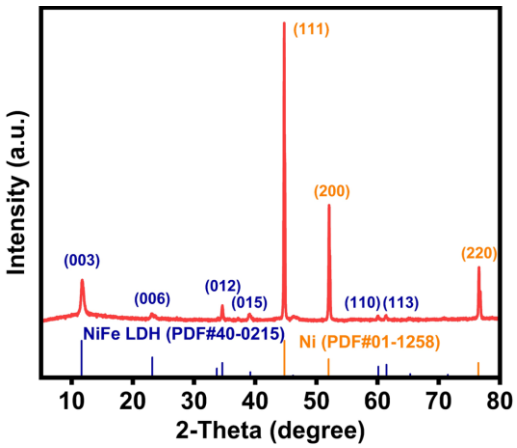

Fig. S39 XRD pattern of homemade NiFe-LDH@NF.

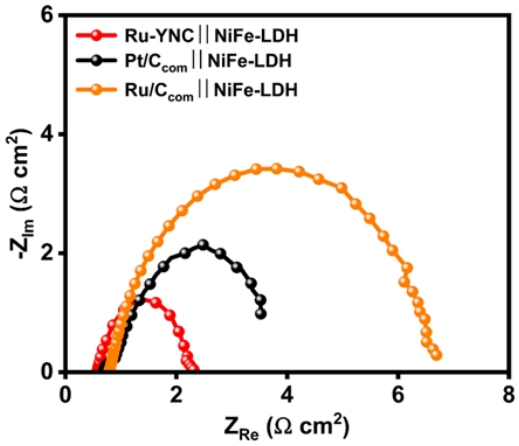

Fig. S40 EIS analysis of the assembled Ru-YNC||NiFe-LDH, Pt/C_{com}||NiFe-LDH, and Ru/C_{com}||NiFe-LDH electrolyzers evaluated at a current density of 0.2 A cm^{-2}.

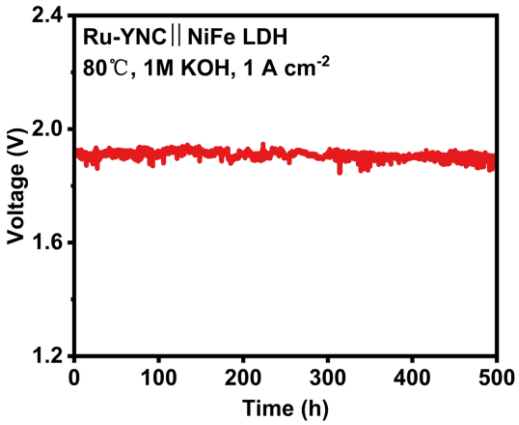

Fig. S41 Stability measurement of Ru-YNC||NiFe-LDH electrolyzer at a current density of 1 A cm^{-2}.

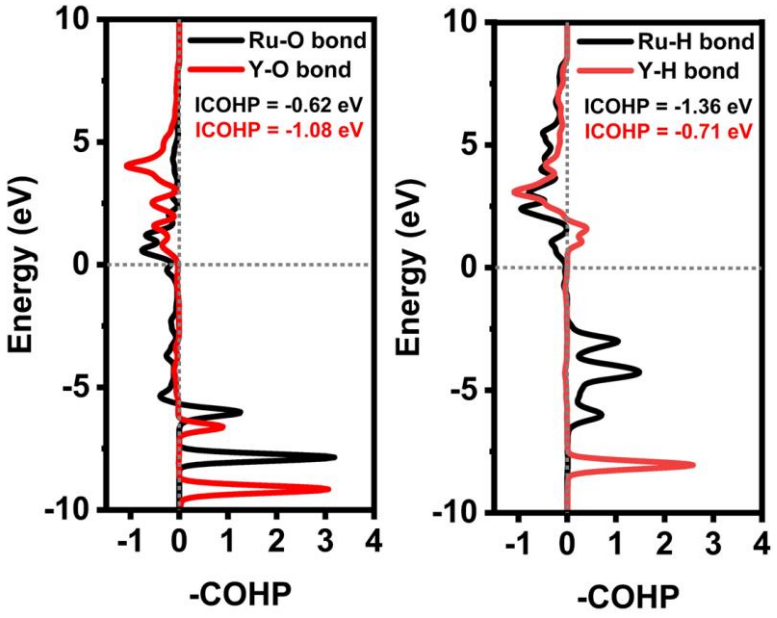

Fig. S42 Calculated COHP of Ru-O, Y-O, Ru-H, and Y-H bonds.

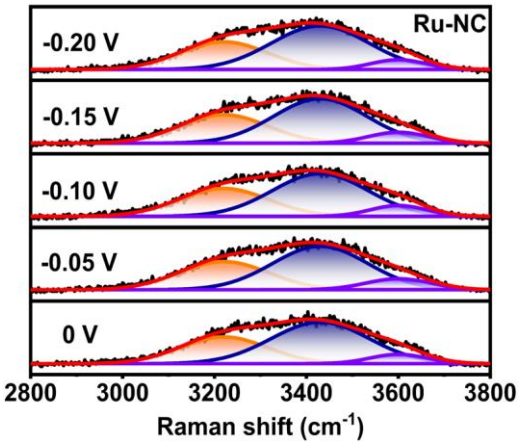

Fig. S43 Electrochemical *in situ* Raman spectra of Ru-NC under different HER bias potentials in 1.0 M KOH solution.

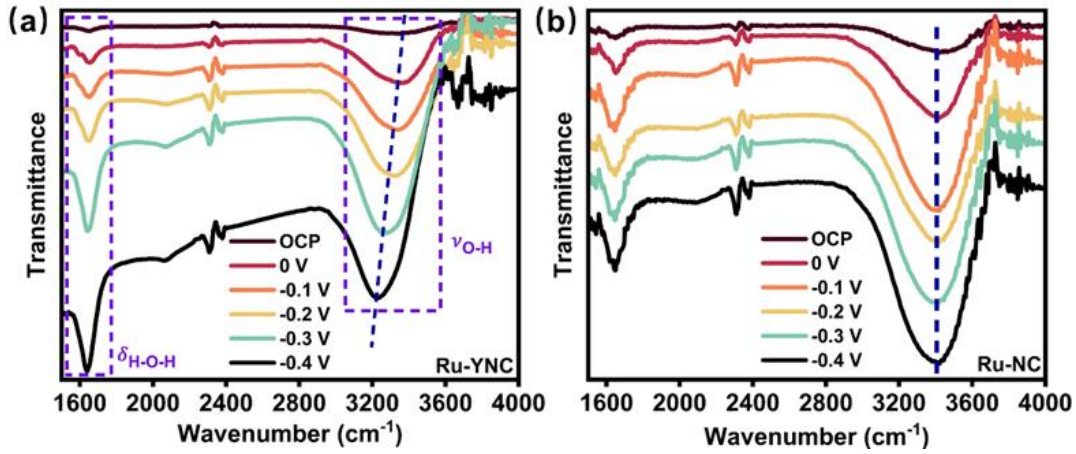

Fig. S44 Electrochemical *in situ* ATR-SEIRAS results of (a) Ru-YNC and (b) Ru-NC under different HER bias potentials.

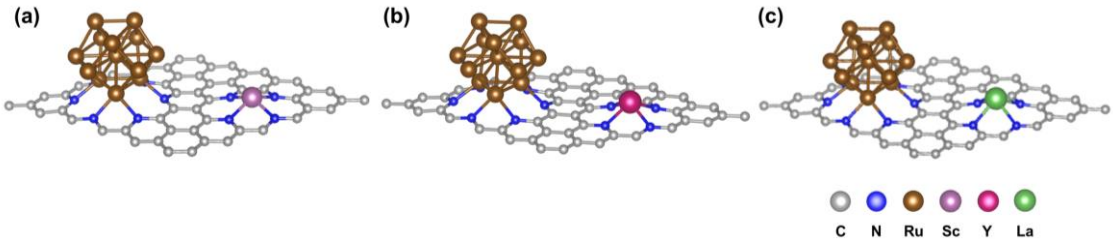

Fig. S45 Optimized theoretical structure models of (a) Ru-ScNC, (b) Ru-YNC, and (c) Ru-LaNC in the side view.

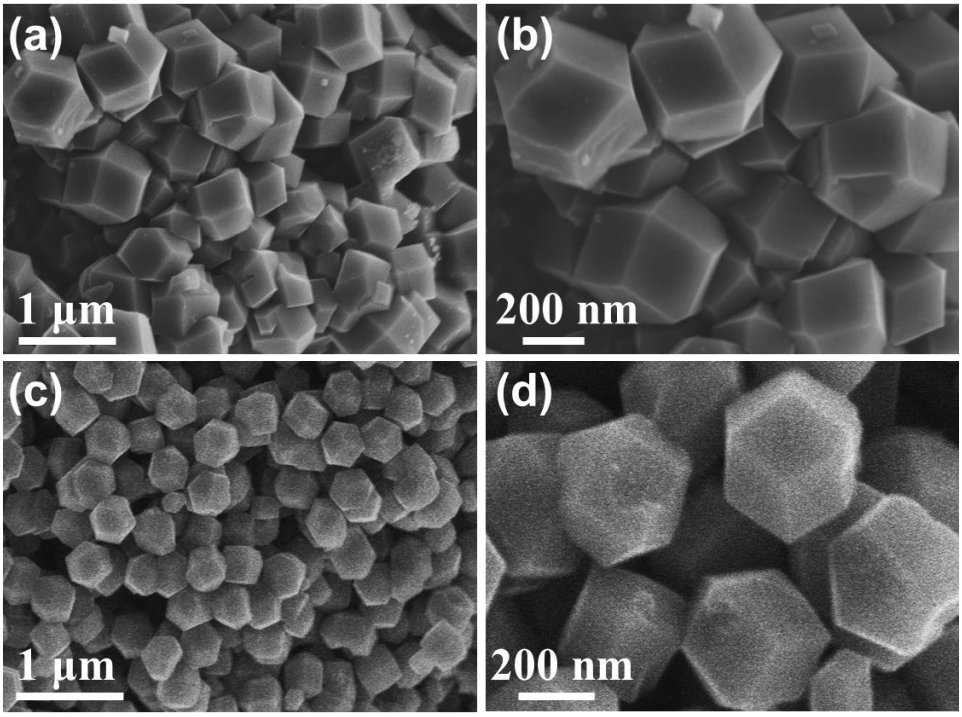

Fig. S46 SEM images of (a, b) Ru-ScNC and (c, d) Ru-LaNC.

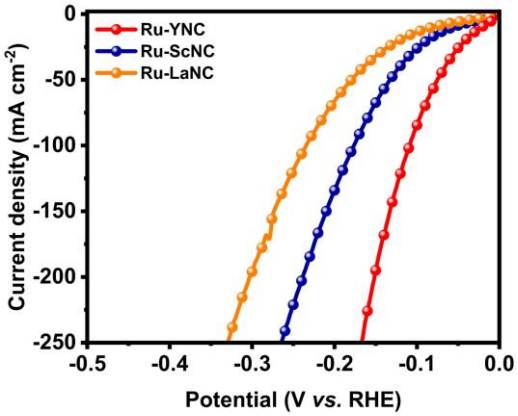

Fig. S47 LSV curves of Ru-ScNC, Ru-YNC, and Ru-LaNC in 1.0 M KOH solution.

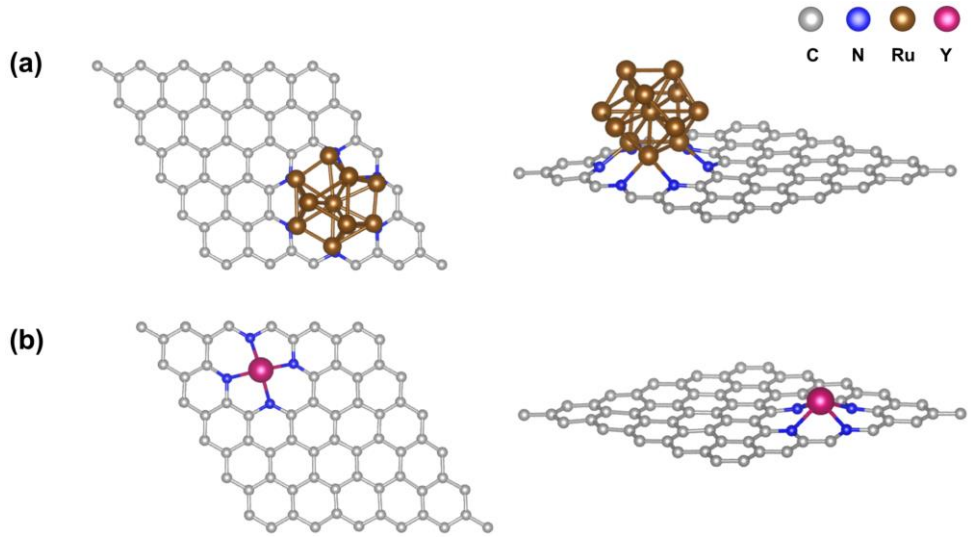

Fig. S48 Optimized theoretical structure models of (a) Ru-NC and (b) YNC in the top and side view.

Supplementary Tables

Table S1 Ru and Y contents in the Ru-YNC, Ru-NC, and YNC measured by ICP-AES.

Sample	Ru content (wt.%)	Y content (wt.%)
Ru-YNC	0.95	0.91
Ru-NC	1.12	/
YNC	/	0.98

Table S2 The relative proportions of the deconvoluted peaks in high-resolution XPS spectra of Ru 3p for Ru-YNC and Ru-NC.

Sample	Deconvoluted peak	Relative proportion (%)
Ru-YNC	Ru^0 $3p_{3/2}$	59.96
	Ru^0 $3p_{1/2}$	85.71
	Ru^{4+} $3p_{3/2}$	40.04
	Ru^{4+} $3p_{1/2}$	14.29
Ru-NC	Ru^0 $3p_{3/2}$	54.98
	Ru^0 $3p_{1/2}$	81.85
	Ru^{4+} $3p_{3/2}$	45.02
	Ru^{4+} $3p_{1/2}$	18.15

Table S3 The positions of the deconvoluted peaks in high-resolution XPS spectra of Ru 3p for Ru-YNC and Ru-NC.

Sample	Deconvoluted peak	Position (eV)
Ru-YNC	Ru^0 $3p_{3/2}$	462.4
	Ru^0 $3p_{1/2}$	484.6
	Ru^{4+} $3p_{3/2}$	464.3
	Ru^{4+} $3p_{1/2}$	486.7
Ru-NC	Ru^0 $3p_{3/2}$	462.7
	Ru^0 $3p_{1/2}$	484.9
	Ru^{4+} $3p_{3/2}$	464.6
	Ru^{4+} $3p_{1/2}$	487.0

Table S4 The positions of the deconvoluted peaks in high-resolution XPS spectra of Y 3d for Ru-YNC and YNC.

Sample	Deconvoluted peak	Position (eV)
Ru-YNC	Y $3d_{5/2}$	158.3
	Y $3d_{3/2}$	160.2
YNC	Y $3d_{5/2}$	157.9
	Y $3d_{3/2}$	159.8

Table S5 EXAFS fitting parameters at the Ru *K*-edge for Ru foil, Ru-YNC, Ru-NC, and RuO_2.

Sample	Shell	C.N.	*R* (Å)	$\sigma^2 \times 10^3$ (Å^2)	ΔE_0 (eV)	*R* factor	S_0^2
Ru foil	Ru-Ru	12*	2.67 ±0.01	3.8 ±0.4	-3.1 ±0.9	0.004	0.907
Ru-YNC	Ru-N	1.5 ±0.3	2.00 ±0.01	4.2 ±1.2	-2.8 ±1.3	0.005	0.824
	Ru-Ru	5.7 ±1.1	2.67 ±0.01	1.8 ±0.6			
Ru-NC	Ru-N	1.3 ±0.5	1.99 ±0.01	4.1 ±0.3	4.5 ±1.1	0.007	0.876
	Ru-Ru	6.8 ±0.9	2.68 ±0.01	2.9 ±1.2			
RuO_2	Ru-O	1.9 ±0.4	1.96 ±0.01	2.7 ±0.8	-5.1 ±1.6	0.009	0.906
	Ru-Ru	7.4 ±1.2	3.14 ±0.02	7.8 ±2.4			
	Ru-Ru	3.3 ±0.6	3.52 ±0.02	2.6 ±1.3			

C.N. is the coordination number; *R* is the interatomic distance (the bond length between central atoms and the surrounding coordination atoms); σ^2 is the Debye-Waller factor (thermal and static disorder in absorber-scatterer distances); ΔE_0 is the edge-energy shift. *R* factor is used to assess the goodness of the fitting. * represents the value that was fixed during the EXAFS fitting. S_0^2 is the amplitude attenuation factor. S_0^2 was fixed between 0.800 and 1.000 during the data fitting. A reasonable range of EXAFS fitting parameters: $0.600 < S_0^2 < 1.000$; C.N. > 0; $\sigma^2 > 0$ Å^2; $|\Delta E_0| < 10$ eV; *R* factor < 0.02.[3,4] It is evident that the coordination number of Ru-Ru in Ru-YNC (5.7) has decreased relative to that in Ru-NC without Y SAs (6.8), which can be ascribed to the fact that the particle downsizing of Ru clusters significantly decouples the Ru-Ru bond.

Table S6 EXAFS fitting parameters at the Y K-edge for Y foil, Y_2O_3, YNC, and Ru-YNC.

Sample	Shell	C.N.	*R* (Å)	$\sigma^2 \times 10^3$ (Å^2)	ΔE_0 (eV)	*R* factor	S_0^2
Y foil	Y-Y	6*	3.59±0.01	4.8±0.3	-2.83±1.6	0.008	0.896
	Y-Y	6*	3.72±0.01	4.5±0.2			
Y_2O_3	Y-O	4.7±0.6	2.26±0.01	7.6±1.1	-3.75±1.1	0.012	0.924
	Y-Y	7.2±0.8	3.53±0.01	6.9±1.3			
YNC	Y-N	3.9±0.7	2.40±0.01	3.9±0.8	1.8±1.2	0.011	0.860
Ru-YNC	Y-N	4.2±0.9	2.42±0.01	5.7±1.6	1.5±1.1	0.014	0.821

C.N. is the coordination number; *R* is the interatomic distance (the bond length between central atoms and the surrounding coordination atoms); σ^2 is the Debye-Waller factor (thermal and static disorder in absorber-scatterer distances); ΔE_0 is the edge-energy shift. *R* factor is used to assess the goodness of the fitting. * represents the value that was fixed during the EXAFS fitting. S_0^2 is the amplitude attenuation factor. S_0^2 was fixed between 0.800 and 1.000 during the data fitting. A reasonable range of EXAFS fitting parameters: $0.600 < S_0^2 < 1.000$; C.N. > 0; $\sigma^2 > 0$ Å^2; $|\Delta E_0| < 10$ eV; *R* factor < 0.02.

Table S7 Noble metal loadings of carbon-paper-supported Ru-YNC and control electrode materials.

Samples	Noble metal loading (μg cm^{-2})
Ru-YNC	4.75
Ru-NC	5.60
Pt/C_{com}	100
Ru/C_{com}	25

Table S8 Comparison between the electrochemical alkaline HER performance of Ru-YNC and recently reported representative noble-metal-based catalysts in 1.0 M KOH.

Catalysts	Noble metal loading (μg cm^{-2})	Overpotential at 10 mA cm^{-2} (mV)	Tafel slope (mV dec^{-1})	Noble metal mass activity (A $mg_{noble\ metal}^{-1}$)	References
Ru-YNC	4.75	22	39	17.79@-0.1 V *vs.* RHE	This work
Pt/C_{com}	100	32	42	0.54@-0.1 V *vs.* RHE	This work
Ru/C_{com}	25	85	148	0.52@-0.1 V *vs.* RHE	This work
Ru@Cu-TM	~53	17	32	4.87@-0.1 V *vs.* RHE	5
Ru@Cu-TiO_2/Cu	52	16	23	7.33@-0.1 V *vs.* RHE	6
Ru NPs/TiN	~3.5	28	41	20@-0.113 V *vs.* RHE	7
Ru SAs/WC_x	~10.27	21	~56	17.3@-0.1 V *vs.* RHE	8
Ru/WC_x	11.28	29	43	6@-0.1 V *vs.* RHE	9
Ru/ac-$CeO_{2-\delta}$	~22.92	21.2	~29	7.18@-0.1 V *vs.* RHE	10
Ce_1-Ru_n/NC	/	/	~42	44.3@-0.1 V *vs.* RHE	11
$Ru_{SA/NP}$-PNCFs	34.8	8	~22	1.078@-0.025 V *vs.* RHE	12
Ru/Zn-N-C	25.56	17.6	~44	1.56@-0.05 V *vs.* RHE	13
Ru/MoO_{2-x}	~7.17	29	22	3@-0.1 V *vs.* RHE	14
RuNi/CQDs	5.93	13	40	1.68@-0.013 V *vs.* RHE	15
Pt-AC/Cr-N-C	4.3	19	30	7.9@-0.05 V *vs.* RHE	16
2D-PtND/LDH	101.52	23	~32	2.1@-0.05 V *vs.* RHE	17
Pt_1/Mn_3O_4	73	24	54	0.374@-0.05 V *vs.* RHE	18
Pt_1/NMHCS	~6.56	40	56	2.07@-0.05 V *vs.* RHE	19

Table S9 Equivalent circuit parameters obtained by fitting the impedance spectra of Ru-YNC, Ru-NC, Pt/C_{com}, and Ru/C_{com} recorded at -0.1 V *vs.* RHE.

Sample	R_s **(Ω)**	R_{ct} **(Ω)**	***T/S s^φ***	***φ***
Ru-YNC	4.097	4.381	0.005	0.796
Ru-NC	4.085	89.400	0.021	0.752
Pt/C_{com}	4.199	6.683	0.009	0.882
Ru/C_{com}	4.182	115.467	0.016	0.817

Table S10 Calculated ECSA values of Ru-YNC and control catalysts.

Samples	**ECSA value (cm^2)**
Ru-YNC	769.1
Ru-NC	217.5
Pt/C_{com}	717.7
Ru/C_{com}	71.3

Table S11 Comparison between the performance of Ru-YNC||NiFe-LDH electrolyzer and recently reported representative noble-metal-based AEMWE devices in 1.0 M KOH.

AEMWE devices	Operate temperature (℃)	Cell voltage (V)	Noble metal mass activity (A $mg_{noble\ metal}^{-1}$)	Stability (h)	References
Ru-YNC||NiFe-LDH	80	1.78@500 mA cm^{-2} 1.87@1000 mA cm^{-2}	52.07@1.87 V	1000@500 mA cm^{-2}	This work
Pt/C_{com}||NiFe-LDH	80	1.90@500 mA cm^{-2}	1.01@1.87 V	/	This work
Ru/C_{com}||NiFe-LDH	80	2.03@500 mA cm^{-2}	2.51@1.87 V	/	This work
Pt@S-NiFe-LDH|| S-NiFe-LDH	80	1.59@100 mA cm^{-2}	/	200@500 mA cm^{-2}	20
Pt-AC/Cr-N-C|| NiFe-LDH	80	1.78@500 mA cm^{-2} 1.90@1000 mA cm^{-2}	19.9@2 V	100@500 mA cm^{-2}	16
Ru_1-Mo_2C|| NiFe-LDH	65	1.83@1000 mA cm^{-2}	21.1@1.6 V	200@500 mA cm^{-2}	21
Ru/CoSA/CNT|| $NiFeOH_x$	80	1.785@1000 mA cm^{-2}	43.15@1.8 V	100@500 mA cm^{-2}	22
UP-$RuNi_{SAs}$/C|| $NiFeO_x$	70	1.70@500 mA cm^{-2} 1.95@1000 mA cm^{-2}	/	250@1000 mA cm^{-2}	23
Pt_{1+n}/Ni_3S_2||RuO_2	80	1.7@100 mA cm^{-2} 2.0@500 mA cm^{-2}	1.35@2 V	~4.4@100 mA cm^{-2}	24
NA-Ru_3Ni/C|| NA-Ru_3Ni/C	60	2.048@1000 mA cm^{-2}	/	2000@1000 mA cm^{-2}	25
Ru/Ni-N_4C-300|| NiFe-LDH	50	1.72@500 mA cm^{-2}	22.6@2 V	1370@500 mA cm^{-2}	26
Pt SACs-$NiCrO_3$/ NF||$NiFeO_xH_y$/NF	Room temperature	1.51@100 mA cm^{-2}	1.41@1.7 V	100@100 mA cm^{-2}	27
Ru SAs/WC_x|| $NiFeOH_x$-NF	80	1.79@1000 mA cm^{-2}	43.2@1.8 V	190@1000 mA cm^{-2}	8

Table S12 Detailed H_2 production data of the Ru-YNC||NiFe-LDH electrolyzer at current densities of 0.5 and 1.0 A cm^{-2}.

J **(A cm^{-2})**	***E*** **(V)**	**H_2 production rate ($\times 10^{-6}$ mol H_2 cm^{-2} s^{-1})**	**H_2 power out (W cm^{-2})**	**AEMWE electrolyzer power (W cm^{-2})**	**AEMWE electrolyzer efficiency (%)**	**Price per GGE H_2 ($)**
0.5	1.78	2.59	0.63	0.89	70.79	0.93
1.0	1.87	5.18	1.26	1.87	67.38	0.99

References

1 L. Xiao, C. Cheng, T. Yang, J. Zhang, Y. Han, C. Han, W. Lv, H. Tan, X. Zhao, P. Yin, C. Dong, H. Liu, X. Du and J. Yang, *Adv. Mater.*, 2024, **36**, 2411134.

2 X. Kang, F. Yang, Z. Zhang, H. Liu, S. Ge, S. Hu, S. Li, Y. Luo, Q. Yu, Z. Liu, Q. Wang, W. Ren, C. Sun, H.-M. Cheng and B. Liu, *Nat. Commun.*, 2023, **14**, 3607.

3 Z. Kou, Y. Liu, W. Cui, B. Yang, Z. Li, R. D. Rodriguez, Q. Zhang, C.-L. Dong, X. Sang, L. Lei, T. Zhang and Y. Hou, *Energy Environ. Sci.*, 2024, **17**, 1540-1548.

4 X. Liang, Z. Zhang, Z. Wang, M. Hu, D. Cheng, Y. Jiang, H. Ren, F. Shen, S. Yang, X. Yang, W. Jiang, X. Shi, Z. Ma and K. Zhou, *Energy Environ. Sci.*, 2025, **18**, 4302-4311.

5 Y. Zuo, S. Bellani, M. Ferri, G. Saleh, D. V. Shinde, M. I. Zappia, R. Brescia, M. Prato, L. De Trizio, I. Infante, F. Bonaccorso, L. Manna, *Nat. Commun.*, 2023, **14**, 4680.

6 Y. Zuo, S. Bellani, G. Saleh, M. Ferri, D. V. Shinde, M. I. Zappia, J. Buha, R. Brescia, M. Prato, R. Pascazio, A. Annamalai, D. O. de Souza, L. De Trizio, I. Infante, F. Bonaccorso, L. Manna, *J. Am. Chem. Soc.*, 2023, **145**, 21419-21431.

7 J. Zhao, R. Urrego-Ortiz, N. Liao, F. Calle-Vallejo, J. Luo, *Nat. Commun.*, 2024, **15**, 6391.

8 X. Lin, W. Hu, J. Xu, X. Liu, W. Jiang, X. Ma, D. He, Z. Wang, W. Li, L.-M. Yang, H. Zhou, Y. Wu, *J. Am. Chem. Soc.*, 2024, **146**, 4883-4891.

9 X. Chen, C. Chen, M. M. Amjad, D. Sun, B. Sun, K. Zhang, *Appl. Catal. B Environ.*, 2024, **344**, 123644.

10 Q. Qin, H. Jang, X. Jiang, L. Wang, X. Wang, M. G. Kim, S. Liu, X. Liu, J. Cho, *Angew. Chem., Int. Ed.*, 2024, **136**, e202317622.

11 F. Shen, Z. Zhang, Z. Wang, H. Ren, X. Liang, Z. Cai, S. Yang, G. Sun, Y. Cao, X. Yang, M. Hu, Z. Hao, K. Zhou, *Nat. Commun.*, 2024, **15**, 448.

12 Z. Xu, J. Zhu, Z. Shu, Y. Xia, R. Chen, S. Chen, Y. Wang, L. Zeng, J. Wang, Y. Cai, S. Chen, F. Huang, H.-L. Wang, *Joule*, 2024, **8**, 1790-1803.

13 Y. Wan, W. Chen, S. Wu, S. Gao, F. Xiong, W. Guo, L. Feng, K. Cai, L. Zheng, Y. Wang, R. Zhong, R. Zou, *Adv. Mater.*, 2024, **36**, 2308798.

14 C. Li, H. Jang, M. G. Kim, L. Hou, X. Liu, J. Cho, *Appl. Catal. B Environ.*, 2022, **307**, 121204.

15 Y. Liu, X. Li, Q. Zhang, W. Li, Y. Xie, H. Liu, L. Shang, Z. Liu, Z. Chen, L. Gu, Z. Tang, T. Zhang, S. Lu, *Angew. Chem., Int. Ed.*, 2020, **59**, 1718.

16 L. Zeng, Z. Zhao, Q. Huang, C. Zhou, W. Chen, K. Wang, M. Li, F. Lin, H. Luo, Y. Gu, L. Li, S. Zhang, F. Lv, G. Lu, M. Luo, S. Guo, *J. Am. Chem. Soc.*, 2023, **145**, 21432-21441.

17 Y.-R. Hong, S. Dutta, S. W. Jang, O. F. N. Okello, H. Im, S.-Y. Choi, J.W. Han, I. S. Lee, *J. Am. Chem. Soc.*, 2022, **144**, 9033-9043.

18 J. Wei, K. Xiao, Y. Chen, X.-P. Guo, B. Huang, Z.-Q. Liu, *Energy Environ. Sci.*, 2022, **15**, 4592-4600.

19 P. Kuang, Y. Wang, B. Zhu, F. Xia, C.-W. Tung, J. Wu, H. M. Chen, J. Yu, *Adv. Mater.*, 2021, **33**, 2008599.

20 H. Lei, Q. Wan, S. Tan, Z. Wang, W. Mai, *Adv. Mater.*, 2023, **35**, 2208209.

21 T. Chao, W. Xie, Y. Hu, G. Yu, T. Zhao, C. Chen, Z. Zhang, X. Hong, H. Jin, D. Wang, W. Chen, X. Li, P. Hu, Y. Li, *Energy Environ. Sci.*, 2024, **17**, 1397-1406.

22 D. Wang, W. Liu, H. Wang, S. Lu, Y. Li, S. Guo, Y. Xiang, *Adv. Funct. Mater.*, 2025, **35**, 2417976.

23 R. Yao, K. Sun, K. Zhang, Y. Wu, Y. Du, Q. Zhao, G. Liu, C. Chen, Y. Sun, J. Li, *Nat. Commun.*, 2024, **15**, 2218.

24 W. Xia, M. Ma, Z. Li, L. Qiao, K. Chi, X. Guo, T. Liu, D. Wu, D. Cao, D. Cheng, *Appl. Catal. B Environ.*, 2024, **354**, 124074.

25 L. Gao, F. Bao, X. Tan, M. Li, Z. Shen, X. Chen, Z. Tang, W. Lai, Y. Lu, P. Huang, C. Ma, S. C. Smith, Z. Ye, Z. Hu, H. Huang, *Energy Environ. Sci.*, 2023, **16**, 285-294.

26 Q. Zhang, M. Lao, Y. Yu, X. Ma, M. Li, Z. Fei, P. J. Dyson, S. Wang, D. Min, *Adv. Funct. Mater.*, 2025, **35**, 2416071.

27 F. Meng, L. Zhu, R. Li, J. Jiang, Y. Li, Y. Wu, Y. Fan, P. Ren, H. Xu, D. Wang, J. Zhang, M. An, P. Yang, *Adv. Funct. Mater.*, 2025, **35**, 2416678.